2021

Nonlinear Impedance Spectroscopy to characterize Hole Transport and Recombination Dynamics in Organic Semiconductor Devices

Robin Rice
University of Vermont

Nonlinear Impedance Spectroscopy to characterize Hole Transport and Recombination Dynamics in Organic Semiconductor Devices

A Thesis Presented

by

Robin Alexander Rice

to

The Faculty of the Graduate College

of

The University of Vermont

In Partial Fulfillment of the Requirements
for the Degree of Master of Science
Specializing in Materials Science

August, 2021

Defense Date: July 9th, 2021
Thesis Examination Committee:

Matthew S. White, Ph.D., Advisor
Matthew Liptak, Ph.D., Chairperson
Madalina Furis, Ph.D.
Cynthia J. Forehand, Ph.D., Dean of the Graduate College

Abstract

Impedance Spectroscopy (IS) is an increasingly common technique to characterize both solid state and electrochemical systems including solar cells and light emitting diodes (LEDs). However, IS relies on a system response being linear with its input such that a time invariant impedance can be defined. This is usually achieved by a small amplitude input. However, doing so suppresses responses of the nonlinear processes which are of considerable interest to those designing and optimizing these devices, such as charge carrier recombination and space charge effects. This investigation employs the recently developed nonlinear extension to IS (NLIS) based in Fourier analysis of the measured harmonic current such that a nonlinear definition of higher harmonic admittance (inverse impedance) is established [16]. By relating Fourier coefficients of the measured current with derivatives of the voltage specific transfer function we may extract valuable physical parameters of the system in question. Benchmark tests of this technique on systems of known transfer functions will be presented specifically measuring hole mobility from space charge and the diode ideality factor from recombination limited current regimes. Finally, NLIS is used to characterise 2-(7-4-N,N-Bis(4-methylphenyl)aminophenyl-2,1,3-benzothiadiazol-4-yl)methylenepropanedinitrile (DTDCPB), a promising novel intramolecular charge transfer (CT) organic semiconductor (OSC). The first known report of DTDCPB hole mobility is presented.

Acknowledgements

This journey began when I took my first college physics course with Dr. Matthew White in the fall of my senior year of undergrad, my second ever physics course. His enthusiasm with the material, dedication to the students, and especially Physics Questions Fridays called me into beauty of what was then a distant peripheral to paths I thought enjoyable or even possible for myself. I wasn't his best student by far, but for the next three years I would consistently find myself fascinated by this physical description of our universe.

There are scores of people who made this possible, some of which I have the pleasure of naming. Dr. Matthew White, who both catalyzed and sustained the last few years of work with *at least* one hundred "brief", patient meetings to remedy the latest experimental hiccup, conceptual misunderstanding, or existential crisis. I will be eternally grateful for the seemingly endless hours that went into this thesis. It has been an immense honor to work with you.

Dr. Madalina Furis, who gave me a chance to engross myself in this beautiful field with only a couple semesters of physics under my belt. I doubt that I, or perhaps anyone will be able to appreciate just how hard you work to keep the department running. For all that I can and cannot appreciate, I am grateful. I wish you the very best at OU. I also greatly appreciate your dedication to a quality cup of coffee.

Dr. Dennis Clougherty, you are a physics magician. I am consistently in awe. I could not be where I am without your courses, or your office hours. I still remember the class right after the first QM test, "Yes a 50% average, but its all about the slope". You inspire persistence.

Dr. Adrian del Maestro, whose intense passion for python gave me the literal tools

with which I could construct my research. Oh, that I wish I could have taken more than a single course with you.

Dr. Luke Donforth, I count myself lucky to know as kind a soul as yours. Your skill and patience in education bring so much color to this work.

To all the men of 1in4 who in a community of vulnerability, honesty, and love help me deconstruct the Imperialist Capitalist White Supremacist Patriarchy.

Kim, you have been with me for the hardest parts of this journey day in and day out. Your love and support made so much in my life possible, and for that I will be grateful until the last. You will always be in my heart.

My therapist, Keith Smith, whose ability to diffuse and deconstruct rivals the very best. You have shown me the practice of the examined life, moreover a life dedicated to community and healing.

To my mother and sister, whose consistent supply of midnight oil made the logistics of literally the whole show possible, and whom I could not have done this without. You have been there from the start and have given magnitudes more than I have returned. You have given the gift of listening, reassuring, guiding, and of course reminding with consistency and grace beyond what is expected. I am privileged to be born into such a persistently loving family. I hope to be there for you as you have for me.

Finally, to David, Johnny, Grayson, Audrey, Sanish, Ekraj, all the other graduate students, and everyone I haven't named I had the pleasure of sharing community with. You are all such wonderful people, it has been an honor to work along side you.

Table of Contents

List of Figures

Chapter 1

Introduction

The success of the semiconductor has relied on the preceding advances in its fundamental physical theory, including Wilson's Band theory, Mott, Davydov and Schottky's contact phenomena theory, and Frenkel and Ioff's photoeffect and tunneling theories, to name a few [28]. Further, the development and consequent success of the crystalline Silicon solar cell was the fruit of decades of intense consistent research focused on reducing loss in every facet, reaching efficiencies of 26% as recently as 2017 [11]. Organic semiconductors (OSC), including devices thereof such as organic photovoltaics (OPV) currently find themselves in the heat of their transition with power conversion efficiencies approaching 18% [26][42] since their introduction in 1986 by Tang et al. [29].

Yet, the rapid expansion of solar technology relies not solely on increased efficiencies, but critically in lowing costs [31]. The drastic departure of OPV technology from silicon make for vast advantages in commercial production and as such represent the next generation of low cost solar.

To usher continual reduction in both efficiency losses and cost requires a host

of powerful analytical techniques. One technique ripe for innovation is Impedance Spectroscopy (IS). Having been in development since the turn of the 20^{th} century, the research community has recently recognized the inherent limitations in a linear analysis of nonlinear systems as various nonlinear extensions of IS, especially within the field of electrochemistry, have been reported over the past two decades [36][14][27]. However, a rigorous mathematical nonlinear extension of IS has only recently been developed by Lai et al [15]. This work aims to further validate that framework, coined nonlinear impedance spectroscopy (NLIS).

This manuscript begins by reviewing the fundamental physics of OSC devices. Next, we establish the critical importance of IS in the study of OSC devices, followed by a review of previous attempts to extend this analysis into the nonlinear regime, a presentation of the developed framework and its advantages over past work. Finally, the results from a series of experiments to validate said framework using known systems, and an application of NLIS to a new promising single layer OPV are presented.

The long-term goal of this work is to develop the presented frequency domain analysis to examine the dynamics of nonlinear processes beyond the dc limit. To establish the presented frequency domain analysis of nonlinear processes in context of the current literature, we compare measurements in the frequency domain at the dc limit with previously reported IS measurements in the linear response regime. By bridging IS with nonlinear processes in the frequency domain, future work will be able to focus on further understanding the reliability and constraints of the presented nonlinear analysis, especially near the high frequency detection limit of the employed experimental setup. Thus, future experiments may be designed with dynamics scaled intentionally within that range (by temperature modulation, etc.)

The extensive literature on mobility measurements from the space charge limiting current (SCLC) regime, as well as measurements of recombination dynamics in amorphous OSC heterojunction devices make OSC devices and materials an excellent test case for the presented nonlinear frequency analysis such that we can confidently compare frequency domain results with previous observations in the dc limit. A brief review of OSC and their electrical properties will be presented which includes a discussion of the electronic configuration of OSC, excitonic OSC, charge transport in small molecule amorphous solids, OSC heterojunctions, and finally SCLC and recombination processes typical of OSC planar heterojunction devices. Carrier mobility, recombination behavior, carrier lifetimes and more may be extracted from the higher harmonic frequency domain for a wide range of semiconductor materials and devices. Most importantly, this technique is applicable well beyond OSC and the diode or space charge behavior therein.

Chapter 2

Organic Semiconductors (OSC)

Since their inception in the 1980s by Tang and Van Slyke, organic light emitting diodes (OLED) and OPV have made significant inroads in markets dominated by their inorganic counterparts. However, crystalline Silicon photovoltaics for example currently comprise over 95% of solar market driven by competitive cost, lifetime, and efficiency relative to OPV. Yet, OPV are a relatively new development and OPV efficiency and cost are poised to overtake Silicon within the coming decades. To achieve this milestone much is yet to be understood in the interaction of morphological, optical, and electrical properties.

Organic semiconducting solids which comprise molecular crystals, amorphous molecular and polymeric films constitute various organizations of molecular subunits. Organic semiconducting small molecules are hydrocarbons, with selective inclusion of additional heteroatoms, with a characteristic carbon backbone wherein adjacent sp^2 hybridized carbon atomic orbitals overlap to form bonding (σ) and antibonding (σ^*) orbitals. These bonds are generally insulating, while overlap of the p_z atomic orbital produces the characteristic bonding (π) / antibonding (π^*) frontier orbitals

which constitute the conducting orbitals [3].

A molecule's ground state is defined as occupation of all bonding orbitals with two antiparallel electrons up to the highest unoccupied molecular orbital (HOMO), while the antibonding orbitals from the lowest unoccupied molecular orbital (LUMO), and every state of higher energy remains unoccupied. The HOMO and LUMO may be considered analogous to the valence and conduction band edge in inorganic crystalline semiconductors. Promotion of an electron by, e.g. photoexcitation, from the HOMO to LUMO creates an neutral excited molecular state, where an electron excited to an antibonding orbital leaves an empty state in the bonding orbital, constituting a hole. Together these are coined an exciton, which, being oppositely charged, are coupled by an exciton binding energy. The Bohr and critical radius of this exciton distinguish conventional semiconductors (CSC) and excitonic semiconductors (XSC) as discussed in the following section, the latter being typical of OSC materials.

2.1 Excitonic Semiconductors

Given an exciton is a coulombically attracted positive and negative charge it may be modelled as a hydrogen atom where the exciton‘s Bohr radius is the orbital radius of the electron wave function from the positive hole. This electron of mass m_e, has an effective mass, m_{eff}, in a bulk with a specified dielectric constant, ϵ_r where $\epsilon = \epsilon_r \epsilon_0$. Using the ground state Hydrogen atom Bohr radius of r_0=0.53Å, the exciton Bohr radius may be calculated:

$$r_{\mathrm{B}} = r_0 \epsilon \left(m_{\mathrm{e}} / m_{\mathrm{eff}} \right) \tag{2.1}$$

The electron effective mass decreases with delocalization. Both, delocalization and increased charge screening by the bulk increase the exciton Bohr radius, the latter characterized by a higher dielectric constant.

The charge carrier in question becomes free at a critical radius wherein the coulombic attraction transitions below the average thermal energy. Setting coulombic attraction equal to the thermal energy, we can solve for the critical radius:

$$E = (q^2/4\pi\epsilon\epsilon_0)(1/r_c) = k_B T \tag{2.2}$$

$$r_c = (q^2/4\pi\epsilon\epsilon_0 k_B T) \tag{2.3}$$

where E is the exciton energy, q the charge of an electron, ϵ the dielectric constant, ϵ_0 the permittivity of free space, k_B the Boltzmann constant, T the absolute temperature, and r_c the critical radius.

When $r_c > r_B$, an exciton is produced spontaneously, for example by photoexcitation. This is quantified by the parameter γ:

$$\gamma = \frac{r_\mathrm{c}}{r_\mathrm{B}} \approx \left(\frac{q^2}{4\pi\epsilon_0 k_\mathrm{B} r_0 m_\mathrm{e}}\right)\left(\frac{m_\mathrm{eff}}{\epsilon^2 T}\right) \tag{2.4}$$

where $\gamma > 1$ indicates XSC behavior and $\gamma < 1$ indicates CSC behavior. A γ value near 1 would not be sufficiently resolved by this model, though this is rarely the case.

In Fig.2.1, the binding energies as a function of carrier separation in nm are shown. There are two wavefunctions shown localized within the coulomb potential

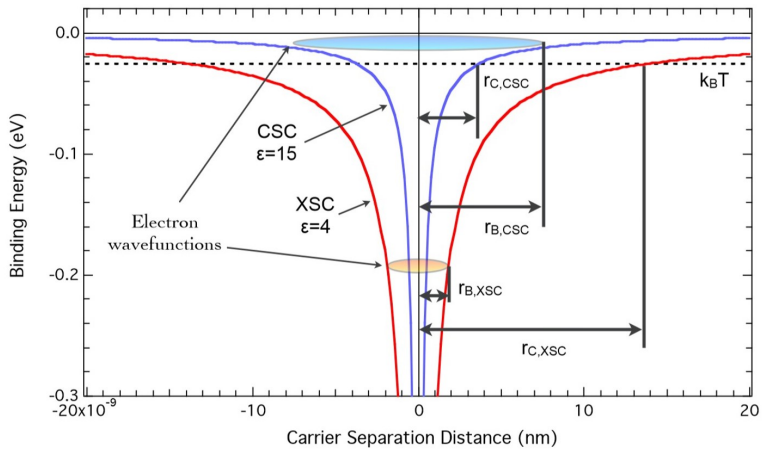

Figure 2.1: The binding energies as a function of carrier separation in nm are shown for the CSC (blue) and XSC (red), note that binding energy decreases as carrier separation increases. Here the dashed horizontal line shows k_BT at some temperature. Figure reproduced by Dr. Matthew White from [12]

well for CSC (blue) and XSC (red) respectively. The thermal energy, k_BT is shown as a dotted black line. Note that as carrier separation increases, i.e. the electron wave function becomes more delocalized, the exciton binding energy decreases. If the carrier separation causes the binding energy to move below k_BT the carriers may be spontaneously dissociated by the thermal energy. As expected, a larger carrier separation is required to reduce the binding energy below the thermal energy for materials of lower dielectric constants such as OSC where the carriers are less effectively screened by the bulk, resulting in an exitonic material. If the wave function fits deeper within the potential well, $\gamma > 1$, indicating excitonic behavior.

Exciton based free carrier generation is intimately tied to the materials charge transport properties. Much of the basis for charge transport in disordered molecular solids lies in the Gaussian distribution model of charge hopping developed by [2] which describes the charge carrier mobility of energetically disordered materials in

Material	σ [meV]	$\sigma/(k_BT)$ (at 298 K)
NPB	76	3.0
TPD	73–76	2.8–3.0
mTDATA	85–112	3.0–4.4
2TNATA	69–71	2.7–2.8
TCTA	75	2.9
P3HT	70–75	2.7–2.9
PCDTBT	130	5.1
DTP-FLU	100	3.9
Spiro-m-TTB	80	3.1
Spiro-TAD	80	3.1
Spiro-TPD	75	2.9
Spiro-MeOTAD	101	3.9

Figure 2.2: Energetic Disorder of various OSCs. Standard deviation, σ, is listed in units of energy (meV) [17].

low field where charge carriers are thermally excited by an energy $\Delta E \sim \sigma^2/k_{\mathrm{B}}T$ from equilibrium:

$$\mu = \mu_0 \exp\left[-\left(\frac{2}{3}\frac{\sigma}{k_{\mathrm{B}}T}\right)^2\right] \tag{2.5}$$

Energetic disorder for common OSCs is listed in Fig.2.2. As the energetic disorder increases, being the variation in the gaussian distribution of the density of states, the energetic barrier to charge hopping increases, and mobility of the solid decreases. However, the 2/3 of Eq.(2.5) were extracted as an empirical fit, and the accuracy of this model has repeatedly been called into question, and consequently many amendments have since been proposed. [35]. Note that this pseudo-classical formula for charge transport in OSCs was proposed only in 1993.

Given the disordered nature of amorphous molecular films, continuous bands do

not form, and charge transfer occurs between localized molecular states. This requires thermal activation of hopping where the energy required to move between localized states depends on the local molecular order, as well as relative molecular orientation and overlap of p_z orbitals in both magnitude and phase, referred to as charge transfer integral overlap [2] [35].

2.1.1 Doping in Amorphous Films

Inorganic semiconductors derive their utility in large part from their ability to be precisely doped such that free carriers are generated in precise concentrations and location [12]. Producing electronic states near band edges (acceptor / donor states), thereby producing free carriers in covalent solids is relatively well understood. The distortion of high energy bonds usually occurs via crystal defects including grain boundaries, or by addition of impurities of different of different valences. The same distortion is difficult in van der Waals solids where intermolecular bonds are low energy and therefore inefficient in producing free carriers, even while chemical and morphological impurity concentrations are generally far higher in van der Waals solids. Regardless, most molecular SC are considered effectively intrinsic.

Adding dopants is complicated by their significant diffusion in amorphous films. Dopants such as O_2, Br, I in a van der Waals solid with a weak lattice will significantly diffuse over time. Even larger dopants like 2,3,5,6-Tetrafluoro-7,7,8,8-tetracyanoquinodimethane (F4-TCNQ) still diffuse too quickly to support a stable p-n junction, which is ultimately destroyed by recombination of dopants and carriers. Rather, doping in molecular OSC is usually chemically or morphologically adventitious which can preferentially trap specific carriers, resulting in an “n-type”

or “p-type” material.

As will be discussed, the exact nature of these trap sites, and or disorder as a whole in disordered semiconductors remains obscure and so, many materials are not specifically designed to be preferential hole or electron conductors but are rather known as having or not having preferential conduction. For example, NPB is a commonly employed as a hole injection or transport layer.

2.1.2 Trap States in Disordered Films

Energetic disorder within amorphous OSC can create shallow trap states within the bandgap either near the HOMO or LUMO causing preferential conduction of charge carriers and subsequent "n-type" or "p-type" behavior. These states near the band edges are caused by pushing the tail states of the localized DOS in OSC of the HOMO or LUMO into the band gap. These tail states then act as shallow trap states.

As will be shown, whether and to what degree a material is an acceptor or donor may be accomplished by design of HOMO and LUMO energy levels, which may be tuned by chemical functionalization. In this way, the energy states and thus the core of charge transport properties of OSCs is opened to the massive synthetic power of organic chemistry.

The DOS describes the energetic distribution of electronic states within energy bands, specifically, the number of states per energy per unit volume. A covalent solid such as c-Si will have a parabolic DOS (Fig.2.3a) with well-defined band edges. As the localization of these states increases, extended states create tails in the band gap, (Fig.2.3b for amorphous Si) which are modelled exponentially. This is seen more clearly in disordered semiconductors with energy states that take a fully gaussian

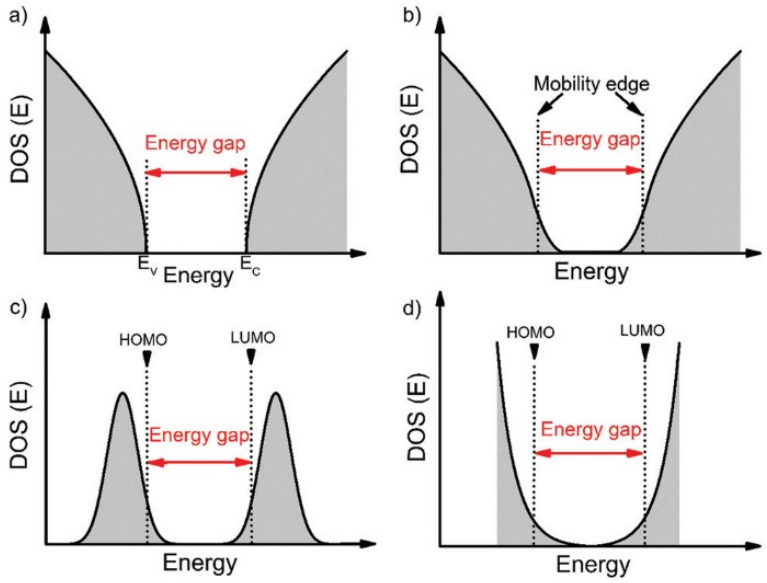

Figure 2.3: The density of states (DOS) for various materials; a) crystalline Silicon, b) amorphous silicon, c) d) amorphous film of small molecule and / or polymeric OSCs. The Energy gap in c-Si is clear as there are very few trap sites, while in disordered solids b)c)d) the mobility edge is used to determine the bandgap. c) shows a gaussian DOS with tail states above and below the HOMO and LUMO respectively. d) shows an abbreviation of the guassian distribution focusing on the tail states within the bandgap. Carriers which are thermally activated to tail states within the bandgap contribute to conduction, while those below and above the HOMO and LUMO are localized. [13].

distribution, which itself can be abbreviated as an exponential distribution (seen in Fig.2.3c and Fig.2.3d for disordered semiconductors). When tail states as signatures of disorder are present, there is no longer a clear band gap and so a mobility edge is used denoting the transition from extended (delocalized) to localized states with an accompanying change in charge carrier mobility. This is shown schematically in Fig. 2.3b as the inflection point of the DOS.

As we shall see, these band tail states are critical to the charge transport properties of disordered materials. However, even though the general form of tail states is accepted a quantitative description of the tail state energy spectrum is unknown for

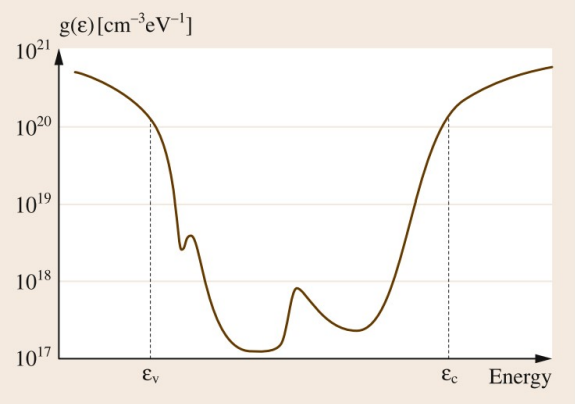

Figure 2.4: The DOS of a non-crystalline semiconductor. E_v and E_c are the mobility edges corresponding to valence and conduction edges, while peaks within the bandgap are likely due to high concentration defect states [1]

most all disordered materials. Without a detailed description of these band states, it is extremely difficult to develop a complete quantitative theory of charge transport in disordered materials, and could be considered one of the principle challenges in the field of disordered OSCs [1]. For example, slow thermodynamic relaxation of disordered materials toward equilibrium which varies by deposition technique, temperature, environmental polarization, etc. can significantly complicate charge transport, especially at low temperatures where electron tunneling between localized states occurs, which is extremely sensitive to the spatial and energetic distance between localized states [1].

Exponential distributions are used to model the extended tail states of localized gaussian DOS distributions of the HOMO and LUMO. A gaussian distribution of deep trap states (red) in the center of the band gap is shown in Fig.2.5 and exponential distributions of disorder induced tail states (black) which extend into the band gap as shallow traps. Once these tail states are extended into the band gap, the tail states are what inform conduction and so the gaussian is often abbreviated by an

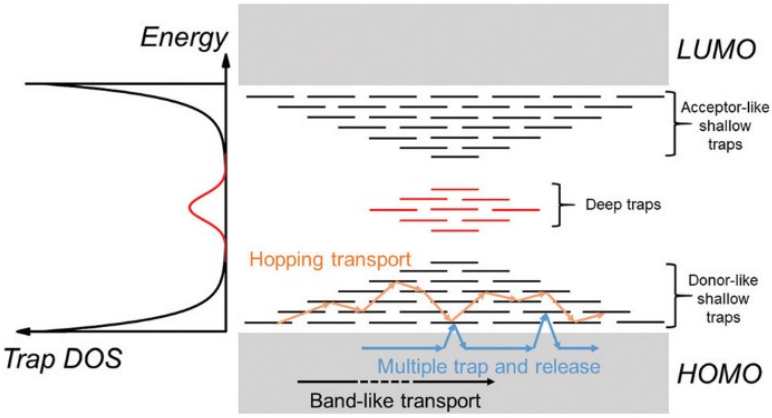

Figure 2.5: Gaussian distribution of deep trap states (red) in the center of the band gap and exponential distributions of disorder induced tail states (black) which extend into the band gap as shallow traps [13].

exponential.

Importantly, if the trap depth, being the energetic distance of trap states from the band edge, is shallow as in localized tail states, they may behave as acceptor or donor-like traps. Shallow traps near above the valence mobility edge, near the HOMO, can behave as donor-like shallow traps. These traps can capture or restrain charge carriers until they are released to the band by external stimulus e.g. electric field, thermal energy, or photoexcitation. The blue arrows of Fig.2.5 show the multiple trap and release (MTR) model where charges moving via delocalized band states are trapped in localized shallow bandgap states and again, while high trap densities allow trapped (localized) charge carriers to move between localized trap states via thermally activated hopping or tunneling, known as charge hopping [13].

Most small molecule amorphous OSC films have a low transfer integral and therefore high energetic barriers for charge hopping between molecules, resulting in low mobility solids and space charge limited current. In fact, most OSC charge carrier

mobilities are below 10 cm^2/Vs while mobilities in crystalline silicon and graphene range in the order of 1×10^3 cm^2/ Vs and 1×10^6 cm^2/ Vs, many magnitudes higher [13]). Consequently, these solids do not have the long-range order typical of most inorganic semiconductors and molecular crystals. Interestingly, as these solids lack long range order, they also lack grain boundaries and therefore exhibit notable mechanical properties including the ability to function if deposited on a flexible substrate. This enables organic electronics to be applied in wearable electronics, bioelectronics, flexible displays and solar panels.

2.2 Space Charge Limiting Current (SCLC)

Space charge limiting current (SCLC) was originally derived by Child and Langmuir in 1910 to describe the motion of charged particles across a vacuum between two parallel plate electrodes of a fixed voltage drop and has since seen extensive modifications to account for unique geometries, quantum mechanical effects, varying charge density, and altered boundary conditions to name a few [10]. The modification considered here was developed by Mott and Gurney in 1940 to describe trap-free SCLC in a solid:

$$J_{\mathrm{SCL}} = \frac{9}{8}\mu_n \epsilon_r \epsilon_0 \frac{V^2}{L^3} \tag{2.6}$$

In terms of mobility, μ_n, applied voltage across the electrodes, V, distance between plates, L, dielectric constant, ϵ_r, and permittivity,ϵ_0, where J gives the current density through the solid film. Both a classical and quantum derivation of the Mott-Gurney

Squared law of SCLC can be found in [10].

In organic solids, the Mott-Gurney law was originally used in high quality single crystals of anthracene / tetracene followed by molecularly doped polymers, and subsequently small molecule amorphous organic solids. This SCLC behavior is observed in solids when the parallel plate electrodes are able to inject a carrier density which overwhelms the free carrier density within the solid, [31]. Appropriate charge injection usually requires ohmic contacts of the electrodes with the solid [4]. Importantly, such a form of current limiting is observable only if charge transport is limited by a single carrier. This also assumes a constant mobility and permittivity of the solid. Notably, the Mott-Gurney law is a trap free form of SCLC model, being that contact defects, impurities, etc. are assumed to be of negligible concentration. While adventitious doping is generally far larger in amorphous OSC than crystalline, the lack of long range order in these solids and weak intermolecular forces means impurity concentrations do not create the shallow states typical of crystalline solids and are likewise not as pertinent to charge transport in amorphous solids. An advantage of the Mott-Gurney law is it does not require that the number of free carriers be known since the number of injected carriers is the theoretical maximum charge density of the film which may be calculated by the film capacitance [12]. The sizeable volume of study dedicated to SCLC especially in OSC films makes it an excellent candidate to compare the frequency spectra of a NLIS measurement with IS in the low frequency bridge.

2.3 Diode Behavior of Organic / Organic Heterojunctions

Although organic / organic (O/O) heterojunciton current-voltage behavior is based in hopping transport between localized excitonic energy states as opposed to the band transport and delocalized free carriers characteristic of inorganic / inorganic heterojunctions, it has been shown [9] that O/O heterojunctions behave roughly according to the Schockley diode equation:

$$I(V) = I_S \left(e^{\frac{V}{nk_{\mathrm{B}}T}} - 1 \right) \tag{2.7}$$

where I_S is the saturation current, n the diode ideality factor, and k_BT is thermal energy. A diode is considered ideal when the diode ideality factor $n = 1$, however for real diodes $n > 1$ according to the type of charge carrier recombination occurring, and of which carrier is recombination limiting.

NLIS will consider the spacing between derivatives of the diode transfer function to extract the diode ideality factor, n, of a device or active layer, bypassing the need to ascribe physical interpretation to the saturation, diffusion, or drift currents of a device. Derivations of the physical interpretation of the diode behavior of O/O heterojunctions [9], energy level alignment of O/O heterojunctions [30], and electrical properties of O/O heterojunctions [19] may be found in literature.

The ability to precisely tune OSC materials by chemical synthesis requires commensurately precise evaluation techniques. IS has been used extensively to evaluate

the electrical performance of OSC devices for decades, with specific focus on SCLC and diode behavior. A brief review of the principles, practice, and limitations of IS will be presented in the next section, followed by presentation of the recently developed nonlinear extension of IS which is the focus of this work.

Chapter 3

Impedance Spectroscopy (IS)

The goal is Impedance Spectroscopy is to define the correlation, if any, between the input and output of the system in question. In the case of sinusoidal inputs, there are four input and output combinations of interest (defined by W. Lai et. al. [15]): i) single sine input to single sine output, ii) single sine input to multiple sine output, iii) multiple sine input to single sine output, and iv) multiple sine input to multiple sine output. This investigation will focus on case ii): a single sine alternating voltage (ACV) perturbation augmented onto a constant direct voltage (DCV) which yields a multi-sine output current. Such a system would conventionally be investigated with linear IS, which warrants a brief overview.

3.1 Theory of Impedance Spectroscopy

IS is a well established method for investigating both electrochemical and solid state systems including batteries, fuel cells, light emitting diodes (LEDs), and solar cells. Impedance was first introduced by Oliver Heaviside to electrical analysis in the 1880s

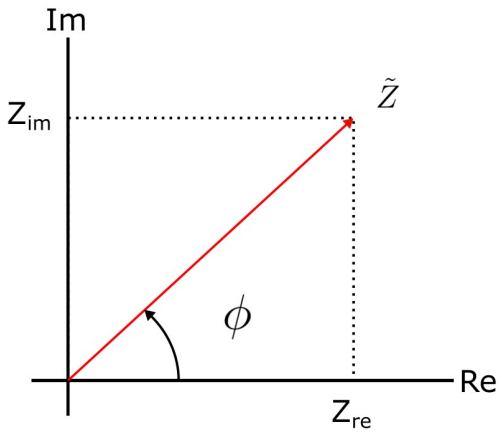

Figure 3.1: Impedance represented as a vector with real and imaginary components on the complex plane

as a phase generalization of resistance. As such, impedance is represented as a vector on the complex plane of complex coordinate,

$$\tilde{Z} = Z_{Re} + iZ_{Im} \tag{3.1}$$

$$|\tilde{Z}| = \sqrt{Z_{Re}^2 + Z_{Im}^2} \tag{3.2}$$

$$\phi = \arctan(\frac{Z_{Im}}{Z_{Re}}) \tag{3.3}$$

$$\tilde{Z}(\omega) = |\tilde{Z}|e^{(i\phi)} \tag{3.4}$$

where $i^a = \sqrt{-1}$, with magnitude, and phase as the positive counter-clockwise rotation from the positive real axis, being the ratio of imaginary to real impedance. The polar to Cartesian coordinate transformation is shown in Fig.3.1. $\tilde{Z}$ is used here to indicate the complex form of impedance, but will be assumed from now on.

[a] j is commonly used in electrical engineering, while physicists tend to favor the use of i. We shall use i so as not to confuse with electrical current density, J.

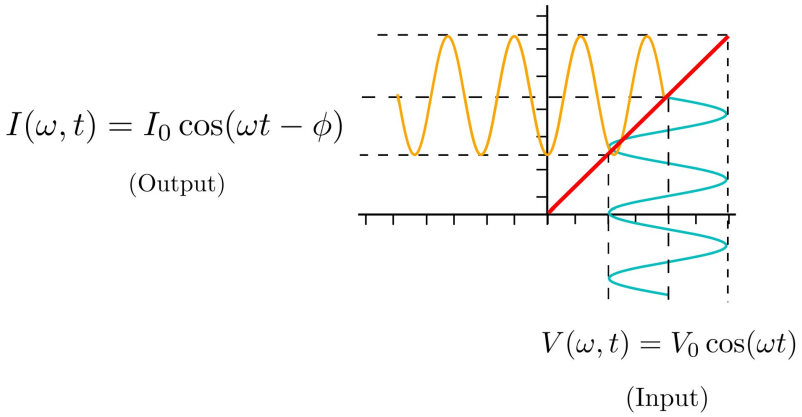

Figure 3.2: In a linear transfer function, a sinusoidal input yields a sinusoidal output with a magnitude and phase shift

Consider a sinusoidal input voltage signal to a system. In a linear system, illustrated by the red line in Fig.3.2, this would produce an sinusoidal AC output with a magnitude and phase shift. Following the Heaviside definition impedance is the ratio of voltage to current.

$$V(\omega, t) = V_o \cos(\omega t) \tag{3.5}$$

$$I(\omega, t) = I_o \cos(\omega t - \phi) \tag{3.6}$$

$$Z(\omega) = \frac{V_o \cos(\omega t)}{I_o \cos(\omega t - \phi)} = Z_o \frac{\cos(\omega t)}{\cos(\omega t - \phi)} \tag{3.7}$$

where $\omega = 2\pi f$. We see that impedance is characterized by a magnitude, Z_o and phase, ϕ. It can be cumbersome however to work in sines and cosines. As a complex number, impedance may be represented on the complex plane using Euler's relation $e^{i\phi} = \cos\phi + i \sin\phi$.

$$V(\omega) = V_o e^{i\omega t} \tag{3.8}$$

$$I(\omega) = I_o e^{i\omega t - i\phi} \tag{3.9}$$

$$Z(\omega) = \frac{V_o}{I_o} \frac{e^{i\omega t}}{e^{i\omega t} e^{-i\phi}} = Z_o e^{i\phi} \tag{3.10}$$

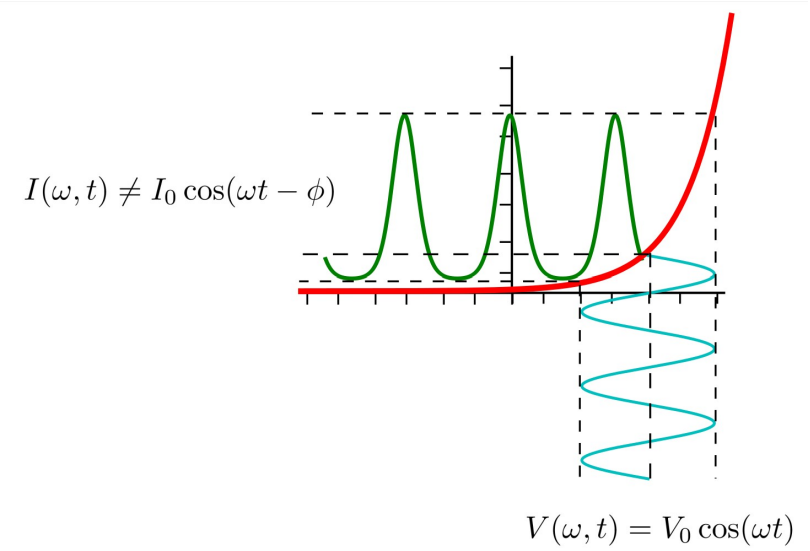

Figure 3.3: A sinusoidal input to a nonlinear transfer function (red) produces an output signal that is periodic but not a pure sinusoidal wave. This output (green) can be deconstructed as a harmonic series by Fourier Transform.

In a nonlinear system, a sinusoidal input produces a periodic though not purely sinusoidal output, as seen in Fig.3.3. A Fourier Transform deconstructs this periodic signal into a series of sinusoidal components, each with their own magnitude and phase, but importantly of sequentially increasing multiples of the input frequency. This series of sinusoidal waves called a harmonic series with each term indicated by its integer multiple of the input frequency, n, (not to be confused with the diode ideality factor), such that in $I(1\omega t)$ $n = 1$, and so it is termed the first harmonic.

In $I(2\omega t)$ $n = 2$, making it the 2^{nd} harmonic, and so on. Since the first harmonic has the lowest frequency, being that of the input, it is frequently referred to as the fundamental term, with fundamental frequency 1ω.

$$V = V_{ss} + V(\omega) \tag{3.11}$$

$$I = I_{ss} + I(\omega) + I(2\omega) + I(3\omega) + \ldots \tag{3.12}$$

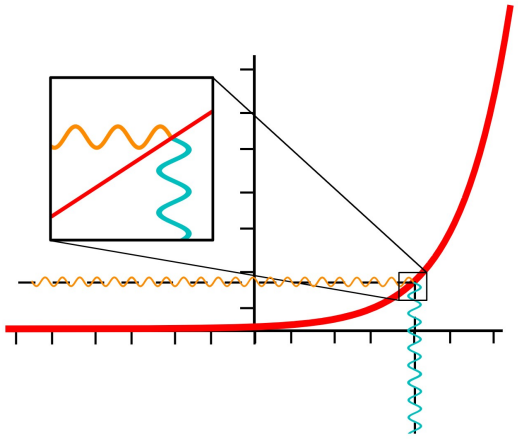

Figure 3.4: As the input step size approaches zero the function appears linear.

Linear IS functions by only considering $I(1\omega t)$, while assuming the magnitudes of higher harmonics are negligible, thereby filtering out the higher harmonics. This process relies on what is referred to as a small amplitude linear approximation. As the magnitude of a sinusoidal input goes to zero any function, including nonlinear functions as seen in Fig.3.4, give an increasingly linear output. That is, the output only changes in magnitude and phase from the input. Linear IS uses this approximation by measuring the output from a small amplitude voltage perturbation across a range of frequencies to fully characterize a system in frequency space. Outside this

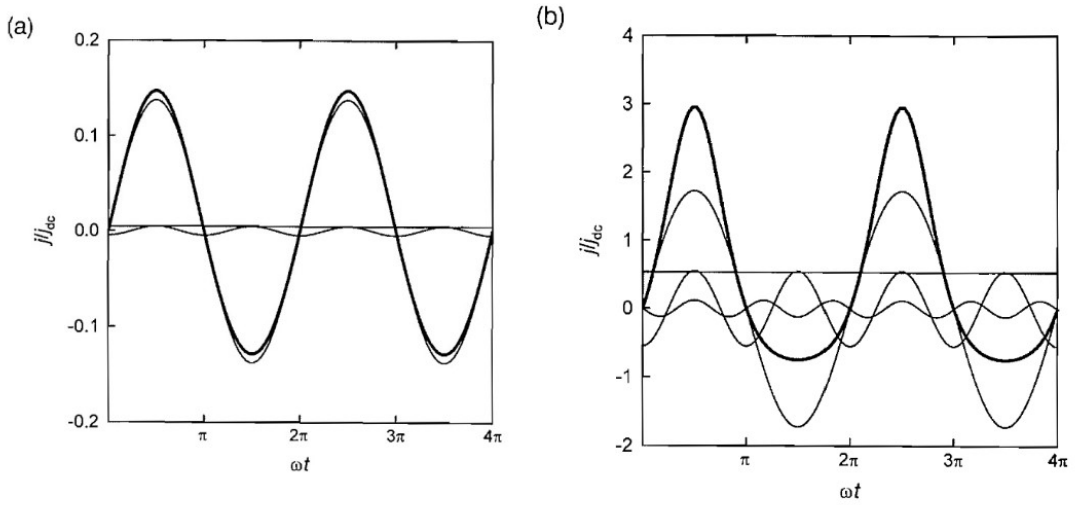

Figure 3.5: Shown are the Fourier components, thin lines, for a total current, bold line, in the case of a simple irreversible charge-transfer reaction. Each figure has a different input voltage magnitude, a) 5mV and b) 50mV.

condition at higher amplitudes, the output resembles what we see in Fig.3.3.

Harrington shows this clearly in a simulated perturbation of a simple irreversible charge-transfer reaction, shown in Fig.3.5, where a) shows a small 5mV perturbation amplitude applied to the system, resulting in an fundamental, the thin line just within the bold line, very closely resembling the total output, being the bold line. Here, the small amplitude linear approximation is valid, while in b) a 50mV perturbation amplitude is used resulting is high nonlinearity of the output. Note that the fundamental $I(\omega)$ is still the dominant component of the total output as it has the highest magnitude. However, the magnitudes of $I(2\omega)$ and $I(3\omega)$ are very significant fractions of the magnitude of the fundamental. The small amplitude linear approximation is not valid in this case.

Even though $I(\omega)$ is dominant in the output of small amplitude perturbations, it is not alone, as can be seen in the 5mV perturbation. Consequently, much care is taken

in Linear IS to choose a perturbation amplitude below the system's characteristic amplitude, above which harmonics of $n > 2$ become significant components of the output. Yet, many of the interesting processes of real systems are nonlinear, and filtering out the higher harmonics suppresses the very nonlinearities which may be most interesting about the system. We shall see further on that nonlinear extensions of IS embrace the higher harmonics by intentionally using a high amplitude perturbation to probe these nonlinear processes directly. Further, if a strategic amplitude and dc offset input are chosen, a system could be fully characterized in a single experiment.

3.1.1 Impedance of Basic Circuit Elements

Every electrical circuit element has a transfer function for voltage to current. Consequently, such circuit elements have unique impedances which we will cover briefly here. Since the current of an ideal resistor is in phase with the voltage, ie. $\phi = 0$, the impedance is purely real, reducing simply to the resistance of the resistor,

$$Z_R = \frac{V_o}{I_o} e^0 = R$$

For a purely capacitive circuit, current, I_c, is the product of Capacitance with the

time derivative of the voltage across the element, V_c.

$$\begin{aligned} V_c(t) &= V_o e^{i\omega t} \\ I_c(t) &= C\frac{dV_c(t)}{dt} \\ &= Ci\omega V_o e^{i\omega t} \\ Z_c &= \frac{V_c(t)}{I_c(t)} \\ &= \frac{1}{i\omega C} = -i\Big(\frac{1}{\omega C}\Big) \end{aligned}$$

thus, the impedance of an ideal capacitor is equal in magnitude to its imaginary impedance. The $-i$ term accounts for the $\frac{\pi}{2}$ phase *lag* of voltage to current in a purely capacitive circuit. Fig. 3.6 shows capacitors have a small real frequency dependent impedance.

For a pure inductor, Z = $i\omega L$. The impedance of an ideal inductor is equal in magnitude to its imaginary component. Likewise The +i term accounts for the $\frac{\pi}{2}$ phase *lead* of voltage to current in a purely capacitive circuit. This may be derived using Faraday's Law: $V_l = L\frac{dI_l(t)}{dt}$

3.1.2 Impedance in Combination

The rules are identical to those for resistances, only using complex numbers.

Series

For components connected in series, the current through each circuit element is the same; the total impedance is the sum of the component impedances.

$$Z_{eq} = Z_1 + Z_2 + \ldots + Z_n \tag{3.13}$$

$$Z_{eq} = Z_{re,eq} + iZ_{im,eq}(Z_{re,1} + Z_{re,2} + \ldots + Z_{re,n}) + i(Z_{im,1} + Z_{im,2} + \ldots + Z_{im,n}) \tag{3.14}$$

Given a Resistor and Capacitor in series,

$$Z_{eq} = Z_R + Z_C \tag{3.15}$$

$$= R + \frac{1}{i\omega C} \tag{3.16}$$

Parallel

For components connected in parallel, the voltage across each circuit element is the same; the ratio of currents through any two elements is the inverse ratio of their impedances.

$$\frac{1}{Z_{eq}} = \frac{1}{Z_1} + \frac{1}{Z_2} + \ldots + \frac{1}{Z_n} \tag{3.17}$$

3.1.3 Randles Circuit

Given a Resistor and Capacitor in parallel,

$$\frac{1}{Z_{eq}} = \frac{1}{Z_R} + \frac{1}{Z_C} \tag{3.18}$$

$$= \frac{1}{R_p} + i\omega C \tag{3.19}$$

$$Z_{eq} = \frac{1}{\frac{1}{R_p} + i\omega C} \tag{3.20}$$

Given a resistor in series with a resistor and capacitor in parallel,

$$Z_{eq} = R_s + \frac{1}{\frac{1}{R_p} + i\omega C} \tag{3.21}$$

This is referred to as a Randles Circuit, commonly used as a basic model for electrochemical systems, most often represented in a Complex Plane Plot of the impedance. The impedance can be further split into real and imaginary components,

$$Z_{eq} = R_s + \frac{R_p}{1 + (\omega R_p C_p)^2} + \frac{i\omega R_p^2 C_p}{1 + (\omega R_p C_p)^2} \tag{3.22}$$

where the Complex Plane Plot behavior becomes more clear. Beginning at low frequencies ($\omega \to 0$), the impedance becomes purely real and the sum of the resistances. As ω increases the 2nd term decreases quadratically with ω while the 3rd imaginary term increases linearly with ω initially until $-Z_{im}$ peaks once $\omega = \frac{1}{R_p C_p}$, and Z_{re} is of equal magnitude offset by R_s. At high frequencies ($\omega \to \infty$) the impedance reduces to that of the series resistance.

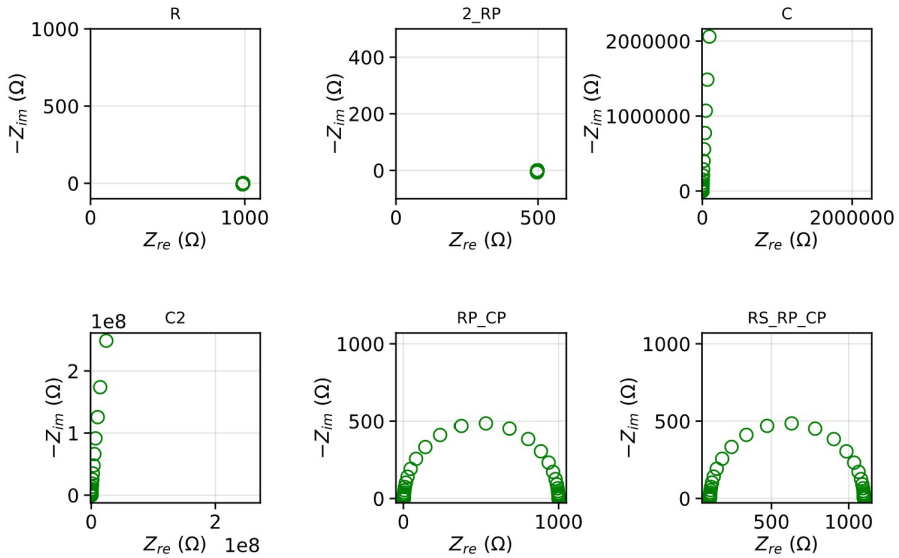

Figure 3.6: Complex plane plot of various circuit elements both isolated and in combination: (from left to right, top to bottom) Resistors being purely real with no frequency dependence, Capacitors being purely imaginary (in theory) with inverse frequency dependence, finally Randles Circuits with real and imaginary frequency dependent impedance are displayed. Figure subtitles indicate circuit element(s)

$$\lim_{\omega \to 0} Z_{eq} = R_s + R_p \tag{3.23}$$

$$Z_{eq}(\omega = \frac{1}{R_p C_p}) = R_s + \frac{R_p}{2} + \frac{iR_p}{2} \tag{3.24}$$

$$\lim_{\omega \to \infty} Z_{eq} = R_s \tag{3.25}$$

3.2 Practice of Impedance Spectroscopy

3.2.1 Equivalent Circuit Analysis (ECA) and Degeneracy

IS investigations typically follow a procedure similar to that described in Fig.3.7 wherein an impedance frequency spectra is measured for a selected system from which a plausible equivalent circuit model is produced based on *a priori* knowledge of the system. The circuit elements represent physical processes of the system such as series resistance of a contact, bulk resistance of a material of interest, parallel plate capacitance, etc. Certain theoretical circuit elements have been created for the purpose of ECA, such as the constant phase element (CPE) resembling a parallel plate capacitor. These elements do not always represent a known physical process, and serve the purpose of fitting an equivalent circuit model to experimental data.

Each circuit element will have a current-voltage transfer function which may be combined with the other elements as described in Section 3.1.2 as an equivalent circuit, with frequency dependent impedance $Z_{ec}(\omega)$. As ECA relies on *a priori* knowledge of the system it is common for multiple equivalent circuits to be made. The simulated impedance spectra of the equivalent circuits are then compared to experiment and a "best fit" model is selected, from which circuit parameters are extracted as characterizing the system in question.

Integral to ECA is the appropriate addition and placement of individual circuit elements to the equivalent circuit. Too few and the equivalent circuit will likely be too simple to fully describe the system, too many and the physical meaning of the ex-

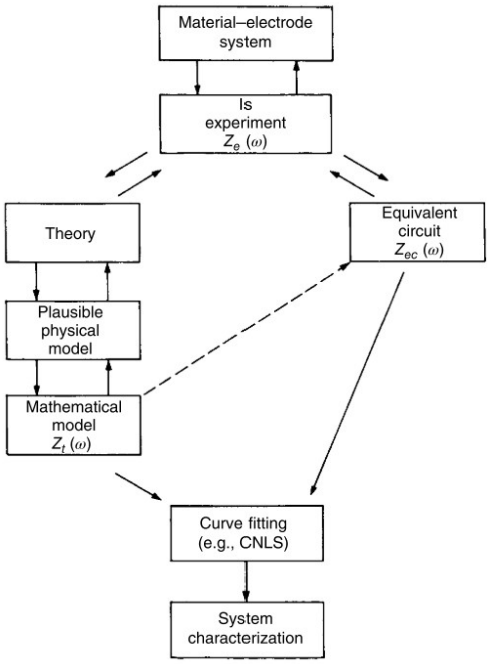

Figure 3.7: Flow chart of typical impedance spectroscopy (IS) experiments and analysis. MacDonald [20]

tracted parameters becomes ambiguous as most any experimental data may be fitted with enough elements, especially theoretical elements. In fact, the problem deepens when considering equivalent impedance transforms which relate multiple equivalent circuits as capable of producing identical, or degenerate impedance frequency spectra. As shall be shown, this has pushed IS beyond use of the fundamental, 1ω, response into higher harmonics with the hope of resolving degeneracy of linear equivalent circuits, in addition to increasing the range of parameters which may possibly be extracted from a system, and increasing experimental efficiency by simultaneous collection of higher harmonics.

3.2.2 Example of LIS - NPB dielectric constant

As an example, I will briefly review the work of Xu et al. [40] to use LIS in extracting the dielectric constant of NPB. Xu et al. [40] employed a combination of J-V measurement and linear IS to investigate the transport properties of NPB in a capacitive ITO/NPB/Al single layer device. A Complex Plane plot was created from the impedance frequency spectra with the form of semicircles with diameter proportional to forward bias. An electrical equivalent circuit was selected in the form of the Randles circuit. Contact resistance, bulk resistance, and bulk capacitance were modelled as series resistance, R_s, parallel resistance, R_p, and parallel capacitance, R_C, respectively.

The Complex Plane plot was normalized as a Modulus spectra revealing a single semicircle with diameter proportional to $1/C$, C being the bulk capacitance based on the device geometry of parallel plate electrodes (ITO and Al) with plate separation d being the thickness of the dielectric NPB layer, seen in Eq.(3.26). The dielectric

constant ϵ_r was calculated using the geometric equation for capacitance,

$$C = \frac{\epsilon_0 \epsilon_r A}{d} \tag{3.26}$$

where A is the area of the parallel plate overlap. The dielectric constant of NPB was found to be 3.6 which is consistent with other values reported in the literature.

Chapter 4

Nonlinear Electrochemical Impedance Spectroscopy (NLEIS)

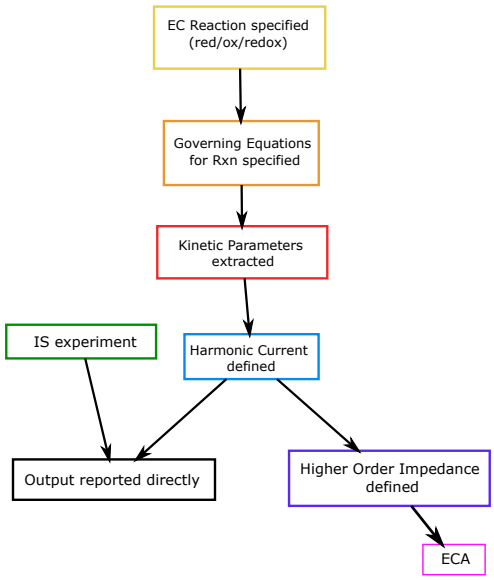

Figure 4.1: Starting from the top, moving down: Flowchart method of features common to NLEIS investigations

In an attempt to resolve the degeneracy among other limitations inherent to IS, nonlinear electrochemical IS (NLEIS) was developed and has seen wider use in the electrochemical field over the last two decades. NLEIS has so far been applied to a variety of systems, as cataloged by Fasmin et al. [8], including fuel cells [33][34], microparticle biomarkers [27], corrosion processes [7][18], li-ion batteries [22] and various other electrochemical (EC) systems. Advantages of NLEIS include high nonlinear response resolution in frequency space[a], a much higher signal-to-noise ratio due to Fourier analysis, and lower requirements for system stability due to simultaneous collection of higher harmonics and given appropriate choice of perturbation amplitude. NLEIS is further able to isolate nonlinear processes in higher harmonics and thus resolve linear degeneracy through higher harmonic response. Consequently, Equivalent Circuit Analysis (ECA) models may be refined.

4.1 NLEIS Procedure

4.1.1 Electrochemical (EC) Reaction

Most all NLEIS investigations concern the kinetics of some electrochemical reaction which is defined at the beginning of the investigation. Fasmin [8] lays out a series of investigations organized by reaction type, most of which are simple electron transfer reactions. Within these are faradaic and nonfaradaic reactions, the later involving some change in electrode composition due to the reaction, rather than providing electrons to a bulk redox reaction.

[a] ie. higher frequency processes are made visible in higher harmonic response, which can resolve nonlinear processes often $\leq 1\%$ the strength of the fundamental response

Reactions investigated are usually very simple single electron transfer reactions. All are reversible redox reactions of various forms: generalized reactions such as reversible redox [36] and adsorption [27]; simple well studied reactions such as the ferri \ferrocyanide redox [39], oxygen reduction [33][34], or Hydrogen evolution reaction [14]; in some cases multiple reactions are studied in parallel [18].

4.1.2 Governing Equations

Once an EC reaction is specified, a governing equation specific to that reaction and the investigated system is selected which serves to relate the sinusoidal input to a (nonlinear) output which are therefore used to develop a nonlinear analysis. Most commonly the Nernst [27][36] or BV [7][39] equations are used which relate a time dependent perturbation to a current via bulk electrolyte or electrode surface species concentrations. Some authors choose to develop a non-standard governing equation based on electrode surface vacancy sites [18][14], or a dimensionless form of the former [33][34].

Butler-Volmer (BV) Equation

The BV equation, Eq.(4.1), describes dependency of electrical current through an electrode on the voltage difference of the electrode and bulk electrolyte for a simple, unimolecular redox reaction, assuming the cathodic and anodic reaction occur on the same electrode. The charge transfer rate, being the rate of the chemical reaction, and mass transfer rate, the rate reactants are provided and products removed from the electrode, limit reactions at the electrode. Mass transfer encompasses diffusion, migration, and convection.

Here, J is the current density in $[A/m^2]$,J_0 exchange current density $[A/m^2]$, c_o^* and c_r^* are the bulk electrolyte concentrations of the oxidized and reduced species respectively, $c(0,t)$ the time dependent concentration zero distance from the electrode surface, α the anodic and cathodic charge transfer coefficient respectively (dimensionless), R the gas constant, T absolute temperature (K), F Faraday's constant, n the number of electrons in the electrode reaction, n overpotential ($n = E(t) - E_{eq}$, where $E(t)$ the time dependent perturbation (potentiostatic, [V]), E_{eq} equilibrium potential).

The extended BV Eq.(4.1) expresses current as a function of potential, n, and concentrations, while the simplified BV equation assumes the bulk electrolyte concentrations to be equal to the electrode concentrations, thus current becomes a function of potential alone.

$$J = J_0 \left[\frac{C_o(0,t)}{C_0^*} \exp\left[\frac{\alpha_a n F n}{RT} - \frac{C_r(0,t)}{C_r^*} \exp\left[\frac{\alpha_c n F n}{RT} \right] \right] \right] \tag{4.1}$$

Nernst Equation

The Nernst equation Eq.(4.2) accounts for concentrations a distance, x, away from the electrode surface.

$$C_o(x,t) = C_r(x,t) \exp\left[\frac{nF}{RT} (E(t) - E_{eq}) \right] \tag{4.2}$$

Given a sinusoidal input Eq.(4.1) and Eq.(4.2) may be expanded by Fourier series

Eq.(4.3) using modified Bessel functions of the first kind as coefficients, I_{2n}, I_{2n+1}.

$$e^{x\sin(\omega t)} = I_0(x) + 2\sum_{n=0}^{\infty}(-1)^n I_{2n+1}(x)\sin[(2n+1)\omega t] + 2\sum_{n=1}^{\infty}(-1)^n I_{2n}(x)\cos[2n\omega t] \tag{4.3}$$

4.1.3 Kinetic Parameter Extraction (via Boundary Conditions)

Once Governing equations are specified, in most cases boundary conditions are applied to the governing equation to solve for the relevant kinetic parameters needed to calculate harmonic coefficients for higher order harmonic analysis. These kinetic parameters usually take the form of concentrations when the Nernst or BV relations are used. Other parameters include reaction rate constants.

Kinetic parameters may be determined in a multitude of ways. Some authors explicitly calculate kinetic parameters. Of those authors who define an electrode surface active site concentration [18], θ, (or dimensionless X [33][34]), that function is Fourier expanded into harmonics, coefficients of like harmonics are equated, a system of equations is generated of a size determined by the number of expanded harmonics, and solved numerically, with accuracy proportional to the size of matrix being solved.

Rather than solve with expansions, some authors determine these kinetic parameters after a harmonic analysis has been developed. Lvovich et al. [27] develop a higher harmonic impedance element and via ECA and Complex Nonlinear Least Squares (CNLS) fitting with experimental data to determine kinetic parameters as

fit parameters for the circuit arrangement. Others simply bypass explicitly solving for kinetic parameters. Riley et al. [39] use the simplified BV equation such that potential is not a function of concentration. MacFarlane et al. [36] choose a system such that concentrations have already been solved. Additionally, Harrington [14] both manually sets θ and symmetry factors, β_a,β_c , in addition to referencing these and other kinetic parameters from literature.

4.1.4 Harmonic Current / Output definition

Once the necessary kinetic parameters, if any, are determined the higher harmonic current may be calculated, assuming a potentiostatic experiment. Current is generally defined through these investigations as the movement of charged species. This may take the form of diffusion current of charged innards of lysed microparticle biomarkers [27], Faradaic [36][39] or non-Faradaic currents [18][14] also coined adsorption current. Though termed impedance spectroscopy, most NLEIS investigations report transformed output data directly.

Higher Harmonic Impedance definitions

A handful of authors chose to redefine the fundamental impedance definition for higher harmonics, however there is currently no consensus on the definition of impedance (or admittance) at higher harmonics. There are three main approaches to defining higher harmonic impedance. All of these approaches tend toward extending the Heaviside linear impedance definition ($Z = \frac{V}{I}$) to higher harmonics via the fundamental ratio of voltage to current $Z = \frac{V}{I}$.

Starting with the earliest, MacFarlane et al. [36] define higher order impedance

Eq.(4.4) using a virtual perturbation Eq.(4.5), where m is the harmonic order, and p indicates contributions to lower order terms from each m. Each harmonic output is treated as a response to a virtual perturbation of the same frequency. MacFarlane mentions Eq.(4.6) as an alternative form.

$$Z_p(s_m) = \frac{E_m(s_m)}{i_p(s_m)} \tag{4.4}$$

$$E_m(t) = (\Delta E)\sin(m\omega t) \tag{4.5}$$

$$E_m(t) = (\Delta E)^m \sin(m\omega t) \tag{4.6}$$

Interestingly, Eq.(4.6) was selected by Lvovich [27] in following the method of MacFarlane, though no justification was given.

Though Ripley [39] reports amplitudes of harmonic currents directly, Ripley's graduate student Xu [38] proposed an alternate harmonic impedance definition which closely mirrors the virtual perturbation approach detailed by [36]:

$$Z_{NL}(\omega, E_0) = \frac{\sum_l E_l(l\omega, E_0)}{\sum_n I_n(n\omega, E_0)} \tag{4.7}$$

where $\omega = 2\pi f$ is frequency, E_0 is the perturbation amplitude, E_l and I_n the harmonic perturbation and currents respectively.

Appraisal of Higher Harmonic definitions

Within the EC framework, impedance analysis is generally a means for extracting rate parameters to develop or refine ECA and/or Reaction Mechanism Analysis (RMA)

models for system processes. As such it is unsurprising that it's nonlinear extension similarly attempts to fit within the Heaviside form of impedance and continue to use equivalent electrical circuit models. It should be said that there is value in these models. For example, relaxation times, or time constants, of various processes which remain obscure in the fundamental may be resolved in higher harmonics. Therefore linearly degenerate ECA or RMA models may then be confirmed or rejected by comparing higher harmonic response with experiment. Further, even when impedance is not defined and harmonic currents are reported directly the transfer coefficient α may be extracted by comparing relative amplitudes of higher harmonic responses.

Issues arise when an inherently nonlinear system output, measured as multiple waves of harmonic frequencies, is used in a linear impedance definition which only accommodates amplitude and phase shift from the input. How does one ratio many outputs to one input? The analytical ease and simplicity which popularized the Heaviside impedance likewise define its inherent limitations. MacFarlane attempted to circumvent these limitations by imagining virtual higher order harmonic perturbations to match with each higher order response. In addition to the matching frequency proposed by MacFarlane, Lvovich expands on this by also allowing the amplitude of these virtual perturbations to match the order of the response as powers of harmonic order. Riley expands this further by allowing separate indices for the perturbation and response harmonics. Lvovich succeeds in expanding a Faradaic current into harmonic order though it is unclear how the higher harmonic impedance definition ultimately differs from harmonic current.

Ultimately the issue of interpreting these definitions rests in there physically being no virtual higher harmonic perturbation. However, the concept of expanding the

input is in reality not too far off from the method proposed here. Indeed the crux of the method lies in expanding the specified cosine input, within a Taylor series of the output, by Maclaurin series (itself a special case of the Taylor series). Further similarity is seen in harmonic power of the perturbation amplitude, in W. Lai as $(x_{ss})^{2m}$ with m being the harmonic index.

Ultimately the method proposed here asserts that impedance at its core is not simply a ratio but a transfer function of the input to output. Within this framework the Heaviside form of impedance is simply the $n = 1$ case of higher order information on the transfer function, where the first derivative describes the slope. This is sufficient for a purely linear system, or a linear approximation of a system (see Small Amplitude Perturbation Linear approximation, higher harmonic filtering in Section 3.1). But for nonlinear systems those higher order derivatives, curvature, jerk, etc., are nonzero and thus hold valuable system information. This is especially true for systems with infinite derivatives, (i.e. exponentials, sinusoids) such as diodes, as will be shown in the following sections detailing the nonlinear extension to IS employed for the remainder of this manuscript.

Chapter 5

Nonlinear Impedance Spectroscopy (NLIS)

5.1 Expanding the Transfer Function

To begin the derivation of higher harmonic admittance used in this investigation, we start with our fundamental transfer function Eq.(5.1) which we know is nonlinear.

$$I(\omega, t) = f(V(\omega, t)) \tag{5.1}$$

We can measure this nonlinear current response and perform a Fourier Transform to calculate the Fourier coefficients, such that:

$$I(\omega, t) = \frac{a_0}{2} + \sum_{n=1}^{\infty} A_n \cos(n\omega t - \phi_n) \tag{5.2}$$

where ω is the fundamental frequency, as defined by the input frequency. The frequency analyzer used in experiment measures the complex Fourier coefficients directly. The complex Fourier coefficient represents the coordinate for a vector in the complex plane whose magnitude and phase are the magnitude and phase of the respective harmonic component of the output current. Note that the frequency analyzer used in this work measures $|A_n|$ for all frequencies and ϕ_n for frequencies lower than 1500 Hz if $n > 1$.

Following the procedure in [15][16] the function $f(V(\omega, t))$ may be expanded by Fourier series Eq.(5.3) or about the point (V_{dc}, I_{dc}) by Taylor Series Eq.(5.4),

$$y(t) = A_0 + A_1 \cos(\omega t + \phi_1) + \sum_{n=1}^{\infty} A_{2n} \cos[2n(\omega t + \phi_{2n})] + \sum_{n=1}^{\infty} A_{2n+1} \cos[(2n+1)(\omega t + \phi_{2n+1})] \tag{5.3}$$

$$y(t) = y_{ss} + \sum_{n=1}^{\infty} \frac{1}{n!} \frac{d^n y}{dx^n}\bigg|_{x_{ss}, y_{ss}} [x(t) - x_{ss}]^n \tag{5.4}$$

where the input $x(t)$ has a cosine form and as such cosine power terms are generated which may be likewise expanded.

$$[\cos(\theta)]^{2n} = \frac{1}{2^{2n}} \frac{(2n)!}{n!n!} + \frac{1}{2^{2n-1}} \sum_{k=0}^{n-1} \frac{(2n)!}{(2n-k)k!} \cos[(2(n-k)\theta)] \ \ (n \geq 1) \tag{5.5}$$

$$[\cos(\theta)]^{2n+1} = \frac{1}{4^n} \sum_{k=0}^{n} \frac{(2n+1)!}{(2n+1-k)k!} \cos[(2n-2k+1)\theta)] \ \ (n \geq 0) \tag{5.6}$$

By example of the even power terms, substitution of Eq.(5.5) into Eq.(5.4) yields

$$\sum_{n=1}^{\infty} \frac{(\Delta x_{ss})^{2n}}{(2n)!} \frac{d^{2n}y}{dx^{2n}}\bigg|_{x_0,y_0} \frac{1}{2^{2n-1}} \sum_{k=0}^{n-1} \frac{(2n)!}{(2n-k)k!} \cos[(2(n-k)\theta)] \tag{5.7}$$

$$\sum_{n=1}^{\infty} \cos(2n\theta) \left[\sum_{m=n}^{\infty} \frac{1}{2^{2m-1}(m-n)!(m+n)!} \frac{d^{2m}y}{dx^{2m}}\bigg|_{x_{ss},y_{ss}} (\Delta x_{ss})^{2m} \right] \tag{5.8}$$

where Eq.(5.8) specifies $m = n - k$ as simplification.

At this point, comparing Eq.(5.8) to the even harmonics sum in Eq.(5.3), we can read off the equation for the even Fourier coefficients, A_{2n}. The same can be done for odd Fourier coefficients A_{2n+1},

$$A_{2n} = \sum_{m=n}^{\infty} \frac{1}{2^{2m-1}(m-n)!(m+n)!} \frac{d^{2m}y}{dx^{2m}}\bigg|_{x_{ss},y_{ss}} (\Delta x_{ss})^{2m} \tag{5.9}$$

$$A_{2n+1} = \sum_{m=n}^{\infty} \frac{1}{2^{2m}(m-n)!(m+n+1)!} \frac{d^{2m+1}y}{dx^{2m+1}}\bigg|_{x_{ss},y_{ss}} (\Delta x_{ss})^{2m+1} \tag{5.10}$$

where $\theta = \omega t + \phi_{2n}$ from Eq.(5.3).

The linear admittance definition ($Y = \frac{1}{Z} = \frac{I}{V}$) fails here as it only allows for the output to change in amplitude and phase, not allowing a change in frequency or for a multiwave output. Further, were we to apply the linear admittance definition to higher harmonic current outputs, the resulting admittance would be time dependent, shown in Eq.(5.14). We could extract a time average value, though what would this value represent and its overall usefulness is unclear as it may average out the very nonlinearities we are attempting to resolve.

$$I(\omega,t) = f(V(\omega,t)) \tag{5.11}$$

$$Y = \frac{1}{Z} = \frac{I_1 e^{1i\omega t-\phi_1} + I_2 e^{2i\omega t-\phi_2} + \dots}{V_1 e^{i\omega t}} \tag{5.12}$$

$$\frac{I_1 e^{1i\omega t-\phi_1}}{V_1 e^{i\omega t}} + \frac{I_2 e^{2i\omega t-\phi_2}}{V_1 e^{i\omega t}} + \dots = \frac{I_1}{V_1} e^{-i\phi_1} + \frac{I_2}{V_1} e^{(2i\omega t - i\omega t)-\phi_2} + \dots \tag{5.13}$$

$$= \frac{I_1}{V_1} e^{-i\phi_1} + \frac{I_2}{V_1} e^{i\omega t-\phi_2} + \dots \tag{5.14}$$

Instead, referring to Eq.(5.15) and Eq.(5.16), we define the complex higher order admittance which converges with the higher order derivative at low frequencies.

$$A_{2n} = \sum_{m=n}^{\infty} \frac{1}{2^{2m-1}(m-n)!(m+n)!} Y_{2n}\Big|_{V_{DC}} V_o^{2m} \tag{5.15}$$

$$A_{2n+1} = \sum_{m=n}^{\infty} \frac{1}{2^{2m}(m-n)!(m+n+1)!} Y_{2n+1}\Big|_{V_{DC}} V_o^{2m+1} \tag{5.16}$$

5.1.1 Higher Order Like-parity Contributions to Lower Harmonics

The higher order admittances have a specific order since the lower order harmonic signals receive contributions from higher order like-parity terms. As such the highest order terms of either parity must be calculated first. This is shown clearly in solving for the first four harmonic admittances assuming Y_5 and Y_6 to be negligible.

$$Y_4 = \frac{192}{V_0^4} A_4 \tag{5.17}$$

$$Y_3 = \frac{24}{V_0^3} A_3 \tag{5.18}$$

$$Y_2 = \frac{4}{V_0^2}(A_2 - \frac{1}{48} Y_4 V_0^4) \tag{5.19}$$

$$Y_1 = \frac{1}{V_0^1}(A_1 - \frac{1}{8} Y_3 V_0^3) \tag{5.20}$$

The higher harmonics magnitudes of the AC current also receive contributions from higher order like-parity terms. For example, A_2 contributes to A_0 and so to define A_0 completely, A_2 and its higher order contributions must first be determined. This can be shown analytically by modeling a Mott-Gurney impedance element in parallel with a parallel plate capacitor given a sinusoidal input voltage. The example here assumes $V_{bi} \equiv 0$, in Eq.(7.1). First, we define the sinusoidal perturbation voltage,

$$V(\omega, t) = V_o \cos(\omega, t) \tag{5.21}$$

followed by the Mott-Gurney element, ($K = \frac{9\epsilon\mu_h A}{8L^3}$)

$$I(V(\omega, t)) = \left[\frac{9}{8}\frac{\epsilon\mu_h A}{L^3}\right](V(\omega, t))^2 \tag{5.22}$$

$$= K[V(\omega, t)]^2 \tag{5.23}$$

$$= KV_o^2 \cos^2(\omega, t) \tag{5.24}$$

and a capacitor in parallel to the Mott-Gurney element,

$$I(V) = C\frac{dV(\omega,t)}{dt} \tag{5.25}$$

$$= -CV_o\omega(sin(\omega t)) \tag{5.26}$$

We may define the current through this circuit as the sum of the current through the Mott-Gurney element, I_{MG}, and the capacitive current, I_C. By expanding $\cos^2\theta$ amd $(sin(\theta) = cos(\frac{\pi}{2}-\theta))$ we may simply read off the nth harmonic Fourier Coefficient as the coefficient of each $\cos(n\omega t)$ in Eq.(5.30).

$$I(V)_T = I_{MG} + I_C \tag{5.27}$$

$$= KV_o^2\cos^2\omega t - CV_o\omega(\sin(\omega t)) \tag{5.28}$$

$$= KV_o^2\big[\frac{1}{2} + \frac{\cos(2\omega t)}{2}\big] - CV_o\omega(\sin(\omega t)) \tag{5.29}$$

$$= \frac{KV_o^2}{2}\cos(0\omega t) + \frac{KV_o^2}{2}\cos(2\omega t) - CV_o\omega(\cos(\frac{\pi}{2} - 1\omega t)) \tag{5.30}$$

$$A_0 = \frac{KV_o^2}{2} \tag{5.31}$$

$$A_1 = -CV_o\omega \tag{5.32}$$

$$A_2 = \frac{KV_o^2}{2} \tag{5.33}$$

Likewise, we can solve for each individual Fourier coefficient using Eq.(5.9) which uses the derivative of the current-voltage transfer function.

$$I(V) = K[V(\omega,t)]^2 + C\frac{dV(\omega,t)}{dt} \tag{5.34}$$

$$\frac{dI(V(\omega,t))}{dV(\omega,t)} = 2K[V(\omega,t)] + C\frac{d}{dt}\left(\frac{dV(\omega,t)}{dV(\omega,t)}\right) \tag{5.35}$$

$$= 2K[V(\omega,t)] + C\frac{d}{dt}\left(1\right) \tag{5.36}$$

$$= 2K[V(\omega,t)] \tag{5.37}$$

$$\frac{d^2I(V)}{dV^2} = 2K \tag{5.38}$$

$$\frac{d^3I(V)}{dV^3} = 0 \tag{5.39}$$

We then solve for the second harmonic Fourier Coefficient by substituting Eq.(5.38) into Eq.(5.40):

$$A_2 = \frac{1}{2(0)!(2)!}\frac{d^2I(V)}{dV^2}\Big|_{V_{DC}} V_o^2 \tag{5.40}$$

$$A_2 = \frac{1}{4}(2K)\Big|_{V_{DC}} V_o^2 \tag{5.41}$$

$$= \frac{KV_o^2}{2} \tag{5.42}$$

where we arrive at the same result as in Eq.(5.33).

5.1.2 Hysteresis Loops

We should note that in the devices studied here the current is taking place in a parallel plate capacitor made by the bottom and top electrodes and the insulating organic layers between them. This geometry significantly influences the high frequency harmonic response. As the frequency of oscillation, ω, increases in a capacitor the

imaginary impedance decreases and capacitive current becomes significant. Likewise, at low frequencies inductive current becomes significant. Both capacitive and inductive currents introduce current phase offsets due to charging and consequential hysteresis loops. V_{peak} trails I_{peak} in capacitive current Eq.(5.45), and vice versa for inductive current Eq.(5.46). Given the admittance is a complex number and proportional to the measured Fourier coefficients, the higher frequency admittance is likewise complex with amplitude representing the size of the loop, and phase the orientation. Capacitive and Inductive currents are distinguished by left and right handed, rotating, hysteresis loops, respectively.

$$Z_C = \frac{1}{\omega C} \tag{5.43}$$

$$Z_L = \omega L \tag{5.44}$$

$$I_{AC} = (C\omega)V_o \cos(\omega t) \tag{5.45}$$

$$V_{AC} = (L\omega)I_{AC} \cos(\omega t) \tag{5.46}$$

A hysteresis loop is not a 1:1 function and therefore a derivative can no longer be defined. Thus, the nth order Admittance, Y_n, is defined as a phased vector valid at all frequencies,

$$\lim_{\omega \to 0} Y_n(\omega) = \frac{d^n I}{dV^n} \tag{5.47}$$

such that at low frequencies the Admittance converges with the derivatives of the current-voltage relation [16]. The phase of Y_n describes the rotation of the hysteresis loop relative to the curve. We can now calculate the higher order, high frequency

Admittance, $Y_n(\omega)$, using the measured Fourier coefficients.

Further, within certain devices such as solar cells hysteresis loops will not be symmetric, ie. forward and reverse bias of the device will not produce currents of equal magnitude, due to nonlinear transport processes such as carrier recombination, trapping, and tunneling. In a solar cell, under forward bias the electron and hole recombine and emit light. On reversing bias immediately after, as in a sinusoidal voltage, there will be less current due to that recombination, thus an asymmetric hysteresis loop will result, indicating nonlinear processes. This investigation is limited by equipment sensitivity as the Novocontrol Frequency Analyzer employed in this investigation can only measure the phase below 1500 Hz for $n > 1$. In the Hole Only devices being studied only holes are present and thus hysteresis loops will indicate trapping and tunneling. Given Y_n is analogous to the nth order derivatives, higher order Admittances can provide insight to the nonlinearity of the hysteresis loops via the curvatures of such loops.

5.1.3 Charge Carrier Mobility

The charge carrier mobility of the active layer may be experimentally calculated using Eq.(5.9) with the measured second harmonic Fourier Coefficient, the Mott-Gurney squared law, the dielectric constant of the active layer, and specific device geometries.

By setting $m = n = 1$ in Eq.(5.9) to specify the second harmonic Fourier coefficient,

$$A_2 = \sum_{m=n}^{\infty} \frac{1}{4} \frac{d^2 I(V)}{dV^2}\bigg|_{V_{DC}} (V_o)^2 \tag{5.48}$$

and solving for the second derivative of the transfer function Eq.(7.1),

$$\frac{dI(V)}{dV} = \frac{9}{4} \epsilon \mu A \frac{(V - V_{bi})}{L^3} \tag{5.49}$$

$$\frac{d^2 I(V)}{dV^2} = \frac{9}{4} \frac{\epsilon_r \epsilon_o \mu A}{L^3} \tag{5.50}$$

we can solve for charge carrier mobility,

$$\mu = \frac{16}{9} \frac{A_2}{V_o^2} \frac{L^3}{\epsilon_r \epsilon_o A} \tag{5.51}$$

where A_2 is the measured second harmonic Fourier coefficient, A is the area of the device active layer, L is the device active layer thickness, ϵ_r is the active layer dielectric constant, $\epsilon_o = 8.85 \times 10^{-14} \frac{\mathrm{F}}{\mathrm{cm}}$ is the permittivity of free space, V_o is the voltage perturbation amplitude. This technique was employed to experimentally calculate NPB hole mobilites, discussed in further detail in Section 7.1.

5.1.4 Recombination Limited Current

In addition to charge carrier transport properties, the higher harmonic frequency spectra additionally holds valuable information on charge carrier recombination. Both

the Planar Heterojunction and Organic Light Emitting Diode (OLED) have multiple charge carriers present.

The Planar Heterojunction device uses an NPB / 2,9-Dinaphthalen-2-yl-4,7-diphenyl-1,10-phenanthroline (NBPhen) interface where we expect recombination to occur at the interface. The Organic Light Emitting Diode device uses an NPB / Tris(8-hydroxyquinoline)aluminum (AlQ3) / NBPhen interface in which recombination is expected to occur within the emitter AlQ3 layer which should be faster than interfacial recombination in the Planar Heterojunction. Current limiting in both these devices at high forward bias should follow the Shockley-Diode equation with an exponential dependence of current on voltage. Therefore, we investigate charge carrier behavior of a distinct form from that in the hole-only device at different speeds.

All investigations described thus far use systems with known transfer functions, being the Mott-Gurney Law and Shockley-Diode equation. The ultimate aim of this work is to develop a methodology whereby we may measure interesting material properties of systems with unknown transfer functions.

Chapter 6

Experimental Details

6.1 Materials

NPB, NBhen, and DTDCPB were purchased from Lumtec Corp.; Al and Ag were purchased from R.D. Mathis; LiF and MoO_3 were purchased from Sigma Aldrich and used as received. ITO slides of 15 $\Omega/\square$ resistance were purchased from Kintec. Glass slides were cut to 1 inch squares and subsequently cleaned in an ultrasonic bath in 18MΩ deionized water and Liquinox, acetone, and isopronanol. Finally they were plasma cleaned for 5 min. at $50W$.

6.2 Fabrication

Devices were fabricated using Thermal vacuum evaporation lithography. Hole only structures were fabricated by spin coating and annealing PEDOT:PSS onto an ITO glass substrate, then evaporating MoO_3 (1 nm), NPB (100-300 nm), Ag (100 nm). The PH diode structure was created by evaporating MoO_3 (1 nm), NPB (100 nm),

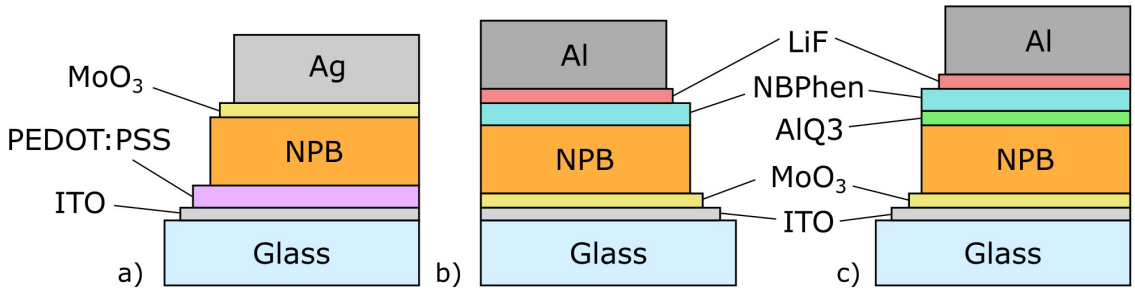

Figure 6.1: Device Structures; a) Hole Only NPB, b) PH diode, c) OLED. Layers are not to scale, though attempt to convey relative thickness.

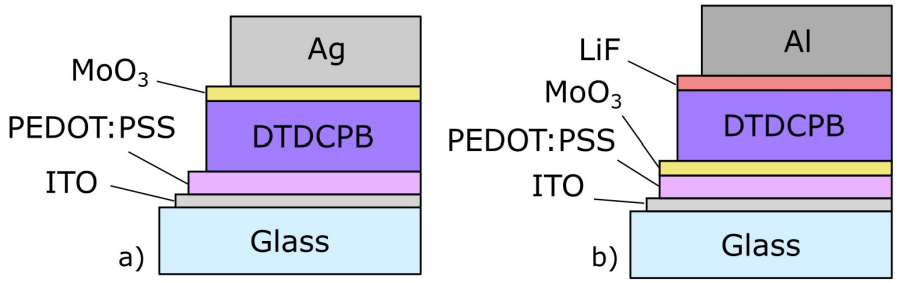

Figure 6.2: Device structures; a) DTDCPB hole only device, b) DTDCPB solar cell. Layers are not to scale, though attempt to convey relative thickness.

NBPhen (20 nm), LiF (1 nm), Al (100 nm). The OLED structure was created by evaporating MoO_3 (1 nm), NPB (100 nm), ALQ_3 (5 nm), NBPhen (20 nm), LiF (1 nm), Al (100 nm) on ITO. Device structures are illustrated in Fig.6.1. The DTDCPB hole only device structures were created by spin coating PEDOT:PSS onto ITO glass substrate and evaporating DTDCPB (100 nm), MoO_3 (1 nm), and Ag (100 nm). The DTDCPB solar cell was fabricated by again spin coating PEDOT:PSS onto an ITO glass substrate and evaporating MoO_3 (1 nm), DTDCPB (100nm), LiF (1 nm), and Al (100 nm). DTDCPB device structures are shown in Fig.6.2. During fabrication and testing these structures were kept in vacuum or nitrogen atmosphere.

6.3 Measurement

A Keithley 2461 Source Measurement Unit was used to measure the JV curve of the device before NLIS measurement. A Novocontrol Alpha-AT frequency response analyzer was used to conduct the nonlinear impedance analysis. AC coupling was used for voltages above 4V DC.

Higher harmonic NLIS spectra taken of a purely linear Randles circuit with element parameters roughly matching the system were used to set the detection limit of higher harmonic measurement. $|An|$ was measured for all frequencies and ϕ_n for all frequencies lower than 1500 Hz if $n > 1$ by the impedance analyzer used. Sampling frequency spectra ranged from 1 MHz to 1 Hz with AC perturbation of 100 mV (root mean square values). The positive terminal was applied to the ITO, and ground to the Al top electrode.

Chapter 7

Results

The investigation of SCLC and electron-hole recombination in OSCs by Larsen et al. [16] introduced the method of NLIS employed in this proposal. However, the systems of study were limited to Metal-Insulator-Semiconductor (MIS) capacitors and PH diodes. In this work, device structures were chosen to isolate charge carrier processes, and iteratively add complexity with each device. Likewise, they were chosen to test multiple transfer function types, and multiple time scales for recombination dynamics. Most importantly, the device structures use well studied materials such that extracted physical parameters may be compared with literature values to check the validity of the NLIS method. The following sections will examine the NLIS investigation of each successive device.

7.1 NPB Hole Only device

The first device we consider is a hole only NPB device, wherein there is no recombination as holes are the only present charge carrier. As shown in Fig.7.1, holes are

injected from the ITO anode into the NPB layer via the spin coated transparent hole injection layer (HIL) PEDOT:PSS. As a soluble HIL, PEDOT:PSS also serves to smooth out ITO surface roughness and locally insulate any short circuits due to that roughness. As another HIL, MoO_3 serves to block electron injection from the Ag cathode while allowing hole conduction. Thus, holes are effectively the only charge carrier present in a hole only device. This allows an isolated study of single charge carrier behavior. Single carrier devices may also be electron only where electron injection layers brace the active layer. Single-layer single-carrier devices such as this are commonly used to isolate material processes [40]. Both PEDOT:PSS and MoO_3 also facilitate improved hole injection from the electrodes to NPB, ensuring Ohmic contact between ITO and NPB wherein current may enter the SCLC regime from which hole mobility may be extracted.

SCLC Hole Mobility

The hole mobility of NPB was extracted within the SCLC voltage regime of high forward bias. In SCLC, the current-voltage transfer function is defined by the Mott-Gurney Squared (MG2) law, Eq.(7.1). $J(V)$ is the current density, $I(V)$ the current, A device area 0.15 cm^2, $\epsilon = \epsilon_r \epsilon_0$ where ϵ_r is the relative dielectric constant, ϵ_0 the permittivity of free space, μ_h the hole mobility, V the applied voltage, V_{bi} the built in potential due to the work function mismatch of the electrodes, L the NPB layer thickness. The complete procedure is detailed in section 5.1.3.

$$J(V) = \frac{I(V)}{A} = \frac{9}{8}\epsilon\mu_h \frac{(V - V_{bi})^2}{L^3} \tag{7.1}$$

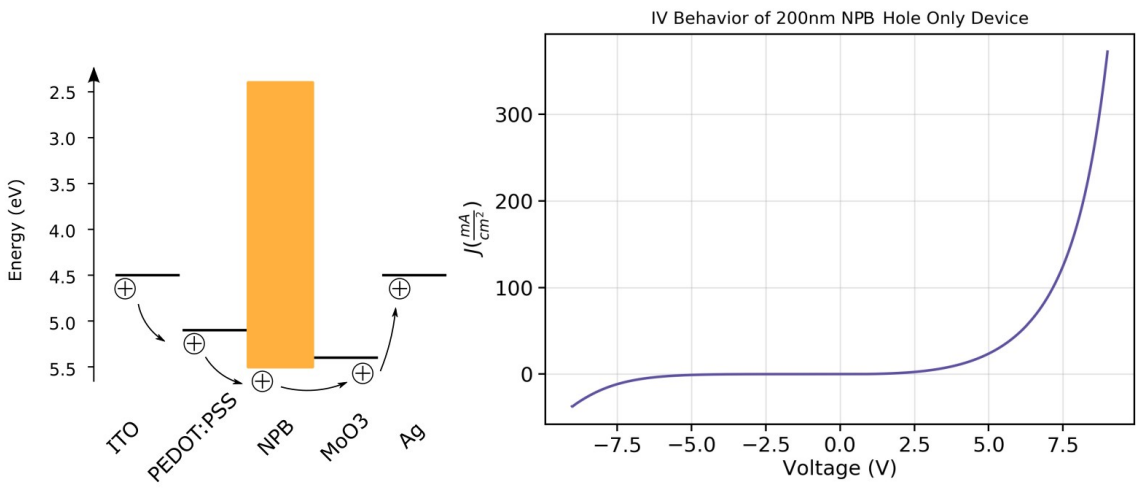

Figure 7.1: Right: Energy band diagram of NPB hole only device showing hole injection from the ITO anode into the NPB layer to the Ag cathode via hole injection layers PEDOT:PSS and MoO_3. Left: JV behavior of a 200 nm NPB hole only device. Note that the current response shows transition from injection to SCLC behavior as there are no electrons present in the device to enable recombination.

SCLC takes place when the charge carrier density of the material reaches its theoretical maximum for that field. Use of SCLC allows for a number of advantages, primarily that it allows mobility to be measured without concurrently needing to know the number of free carriers in the material [12]. In its simplest form, the MG2 law assumes a trap free state. If a system is in fact not in the SCLC regime, mobility will be underestimated as SCLC assumes maximum carrier contribution to the current [31].

Higher Harmonic frequency spectra of NPB Hole Only devices

The higher harmonic current spectra of NPB Hole Only devices, seen in Fig.7.2, show that above 2.0 V forward bias the first two harmonic currents are above the noise floor. It can be seen that A_3 and A_4 are below the noise floor, roughly three orders of

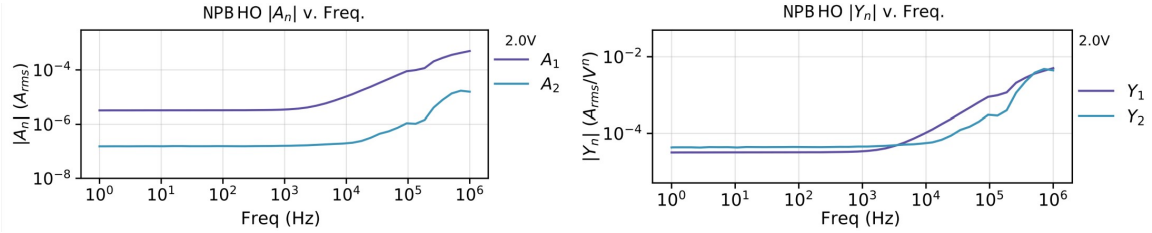

Figure 7.2: NPB Hole Only device (left) magnitude of the measured AC current, $|A_n|$ (A_{rms}), v. Frequency (Hz) for a 100 mV_{rms} amplitude voltage excitation. (right) magnitude of the higher harmonic admittance, $|Y_n|$, likewise. NPB layer thickness = 150 nm. A_ns represent the Fourier coefficients the Measured AC current at ω, 2ω, etc. where ω is the fundamental frequency defined by the AC voltage input signal. The first two harmonics are shown for both higher harmonic current and admittances. A_3 and A_4 were observed to be below the noise floor roughly three orders of magnitude below A_1, and so are not shown.

magnitude below A_1. A signal to noise (SNR) ratio can be determined by measuring the higher harmonic response of a purely linear equivalent circuit model with series resistance, parallel plate capacitance, and bulk resistance comparable to the device structure.

J-V measurements confirm SCLC behavior at this voltage, thus we interpret the significant second harmonic as proportional to the second voltage derivative of the MG2 transfer function. Equating the second voltage derivative of the MG2 law Eq.(7.1) with the measured second harmonic Fourier coefficient we may solve for the hole mobility of NPB directly. Above $\sim 5 \times 10^4$ Hz the second harmonic current fourier coefficient increases. At this frequency capacitive current due to the device geometry becomes significant and the admittance (and the related harmonic fourier coefficient in Fig.7.2) diverges from the constant value of the derivative. Consequently, mobility calculations used an average value of A_2 from $1 - 10$ Hz, where capacitive current is negligible.

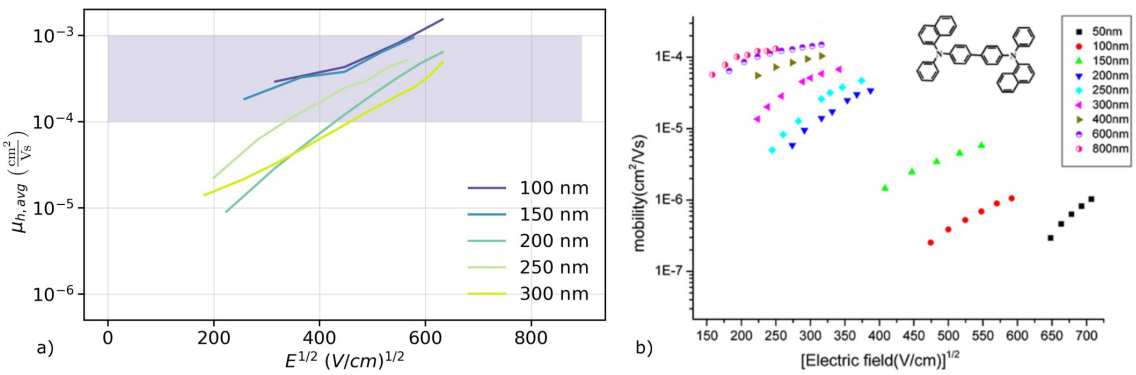

Figure 7.3: a) Hole mobility of the NPB active layer in the NPB hole only device as a function of applied electric field for 100-300 nm NPB layer thicknesses. The shaded region roughly shows the acceptable range for NPB hole mobility. b) Hole mobility of an ITO / NPB(x) / Al single layer device shown as a function of applied electric field by NPB layer thickness, x, adapted from [37].

Hole Mobility of NPB

The extracted hole mobility of NPB, averaged from $1-10$ Hz, is plotted in Fig.7.3 as a function of the square root of the electric field. The mobility data for each device is clipped to show only voltage ranges where a significant A_2 is observed over at least $1-10$ Hz in the frequency spectra, indicating SCLC via the MG2 law. Due to the field dependence of the hole mobility on electric field, the hole mobility of NPB and similar molecules (α-NPB: additional methyl, TPD: toluene in place of naplthalene) is often reported as an order of magnitude from 1×10^{-4} to 1×10^{-3} $\frac{\text{cm}^2}{\text{Vs}}$ [25] [21]. The direct dependence of mobility with electric field is expected as following the Poole-Frenkel model of charge transport in thin films of small molecule amorphous OSCs.

The apparent thickness dependence of NPB hole mobility, seen in Fig.7.3, has been reported previously [37] [5]. Chu et al. attributed the dependency to the presence of deeper trap states within the band gap of NPB at lower films thickness. Fig.7.4 shows the trap energy (eV) and density of trap states, where deep traps are those of higher

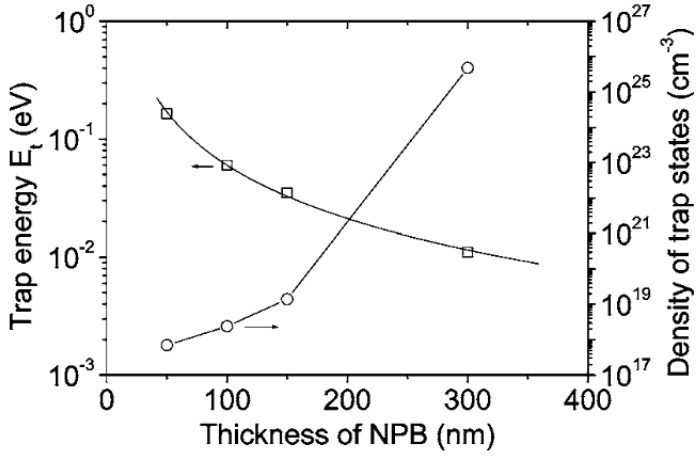

Figure 7.4: Trap energy and density shown for 50, 100, 150, and 300 nm NPB layer thickness within ITO/C60/2.5 nm/NPB(x)/Al devices.[6]

energy compared to shallow traps. Chu proposes that as the trap energy decreases the density of trap states increases with layer thickness and thus the ability of NPB to transport holes increases as holes transport between NPBs trap states and HOMO level. Specifically, Chu notes that as the trap energy dips below $k_BT = 0.0259eV$ at 300 K for an NPB layer thickness of 300 nm the trap states become too weak to significantly influence hole transport.

Though the time-of-flight (TOF) mobility measurement technique is widely viewed as a standard, it requires film thickness of >1000nm for penetration depth of laser to meet carrier flight distance [37]. OLED and OPV designs typically use film thicknesses on the hundreds of nm scale, therefore a mobility measurement technique that operates at comparable thicknesses is desirable.

Further, if we consider both contact resistances as being in series with the resistance of the active layer, as the active layer becomes thin relative to the contacts, the contact resistances become the dominant current limiting process. Therefore, ex-

tracting the mobility using the fundamental harmonic, as in the case of IS, one may be measuring contact resistances. By using the second harmonic however we are no longer measuring resistive processes. We see this qualitatively in the relatively narrow two-order-of-magnitude spread of mobility values by thickness compared to the IS mobility measurements which have a four-order-of-magnitude spread of mobility values with thickness. Note also that Xu et al. do not use HIL in their device, as we have to ensure Ohmic contact and SCLC in the NPB film. Indeed, when injection layers are used [5] [23] a weaker thickness dependence is observed.

Future investigations may also compare other accepted mobility extraction techniques such as linear admittance spectroscopy and time of flight (TOF) with NLIS for the same device. At present, the extracted hole mobility being within the accepted order of magnitude range while exhibiting the expected thickness and field dependence confirms the validity of the NLIS analysis for evaluating hole mobility.

Additionally, as this investigation confirms the bridge between linear and nonlinear impedance spectroscopy via the low frequency limit, future investigations may focus on the interpretation of higher frequency higher harmonic responses. Overall, this series of experiments demonstrates the value of information held in the higher harmonic current response for example in calculating the charge carrier mobility of OSC active layers within the SCLC regime. In the following sections we will explore the same calculation of hole mobility within devices where multiple charge carriers are present, as well as demonstrate the value held in the higher harmonic admittance spectra.

7.2 Planar Heterojunction Diode

SCLC in the PH diode

As recombination is occurring in the PH diode, in order to calculate NPB hole mobility additional criteria must be met. Given this is not a hole only device, electron transport should be considered. But, as stated by Larsen [16], electron transport is not considered to be limiting as the electron transport layer (C60 in that case) was 6x thinner than the hole transport layer (CuPC in that case). For the PH diodes we are studying with HTL and ETL being NPB and NBPhen respectively, the NBPhen layer (20 nm) is 5x thinner than the NPB layer (100 nm), and so the same statement can be made. Given the NPB layer is 5x thicker, transport limited current should reflect transport through NPB. As expected, SCLC NPB hole mobility calculations agree well with an average of 3.5×10^{-4} cm^2/Vs [25], seen in Fig.7.6.

As with the NPB hole only device, the mobility data per each device is clipped to show only voltage ranges where a significant A_2 is observed over at least $1 - 10$ Hz in the frequency spectra, indicating SCLC as a significant second voltage derivative of the MG2 law. Given there is a significant recombination regime at moderate forward bias in the PHD and OLED devices following low forward bias injection limited current, we expect to observe SCLC over a higher forward bias than in the NPB hole only devices. And so, we see mobility extracted from roughly 500-800 $(V/cm^2)^{1/2}$ in devices with recombination as compared with the roughly 200-600 $(V/cm^2)^{1/2}$ range in the NPB hole only devices.

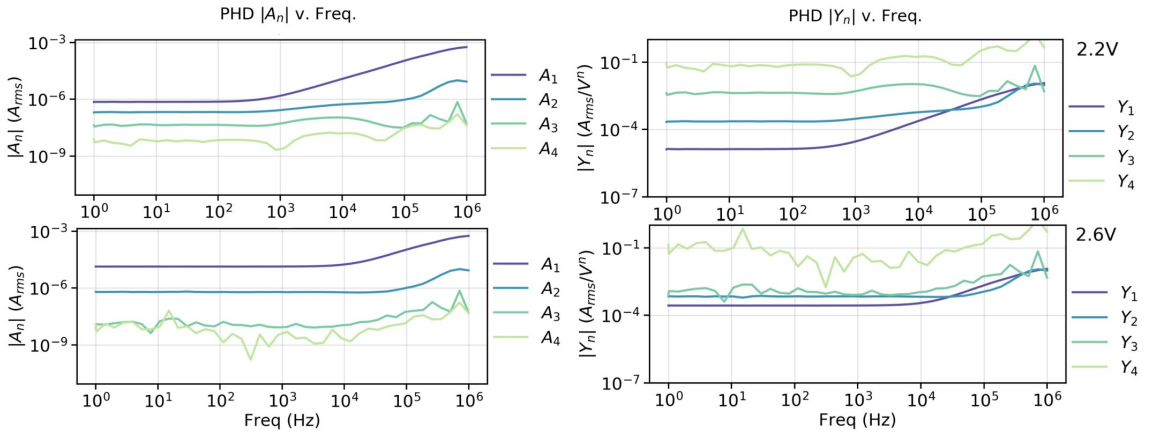

Figure 7.5: PHD device, left: magnitude of the ac current, $|A_n|$ (Arms) v. Frequency (Hz), right: magnitude of the admittance, $|Y_n|$ v. frequency (Hz) for a 100 mV_{rms} amplitude voltage excitation at 2.2 and 2.6 V applied dc bias. Note that in SCLC regime, the first two harmonics currents are constants below 3×10^4 Hz. At this point the admittance diverges from the derivative as capacitive current becomes significant. A_ns represent the Fourier coefficients the Measured AC current at ω, 2ω, etc. where ω is the fundamental frequency defined by the AC voltage input signal. The first four harmonics are shown for both higher harmonic current and admittance.

Validity of NPB Hole Mobility: Discussion of SCLC Measurements

Though NPB is a well studied material, reported values of hole mobility in NPB vary on the order of 10-100 especially when the SCLC regime is used. Blakesley et al. [4] investigated the large standard deviation in SCLC experiment and analysis concerning OSC carrier mobilities for nominally identical materials, specifically for J-V device analysis, and found mobility variation in such devices was attributable mainly to poor electrodes and inconsistent film thickness. As mentioned in Section 7.1, SCLC requires that electrode contacts must be Ohmic, i.e. they are able to sustain bulk limited injection to the organic layer rather than injection limited. However, injection limited current (specifically, those derived from the Richardson-Schottky emission model) show exponential dependence of the current density on the applied field. As

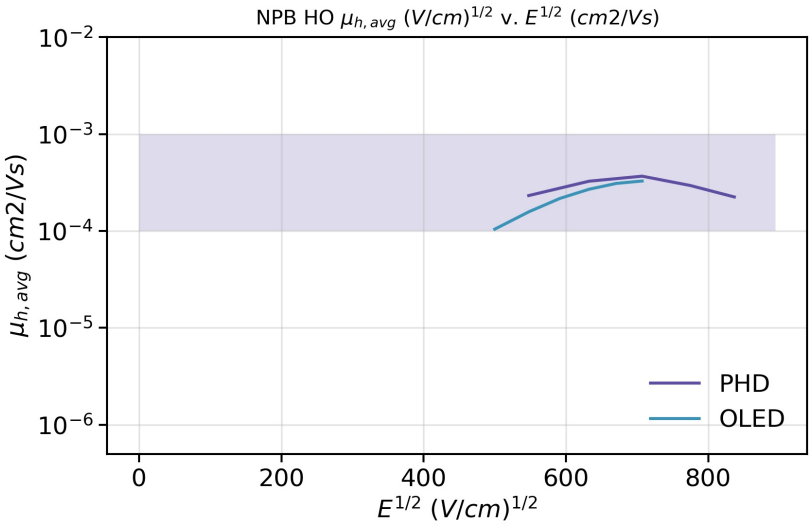

Figure 7.6: Hole mobility of the NPB active layer in both the planar heterojunction diode (PHD) and organic light emitting diode (OLED) as a function of applied electric field. The shaded region shows the acceptable range for NPB hole mobility.

no exponential behavior is observed in the higher harmonic frequency spectra of the Hole Only NPB device and given the vanishing third harmonic fourier coefficient it is very likely SCLC has been reached in the devices presented here.

Next we consider the Planar Heterojunction (PH) diode where both electrons and holes are present via NBPhen electron transport layer (ETL) and LiF electron injection layer (EIL). Consequently the PH diode exhibits both exponential diode behavior at moderate bias and SCLC behavior at higher bias. Within recombination limited current under moderate bias the PH diode is expected to behave according to the Shockley-diode equation, where I_S is the saturation current, n the diode ideality factor, and k_BT is thermal energy. A diode is considered ideal when the diode ideality factor $n = 1$, however for real diodes $n > 1$ according to the type of charge carrier recombination occurring, and of which carrier is recombination limiting.

$$I(V) = I_S \left(e^{\frac{V}{nk_BT}} - 1 \right) \tag{7.2}$$

Recombination Limited Current in the PH diode

In this device electrons are injected from the cathode into the NBPhen via the LiF EIL and transport towards the planar heterojunction interface, as seen in Fig.7.7. Holes are injected into the NPB via the ITO anode and MoO_3 HIL layer and transport towards the planar heterojunction interface.

The PHD device was shown to emit with a peak wavelength of 489.53 nm as shown in Fig.7.7 and Fig.7.8, corresponding to a 2.48 eV transition. NPB is reported to show photoluminesence at 2.75 eV (450 nm) in solution. It is possible however, that crystallization reduces the band gap of NPB compared to solution. Interfacial recombination however, between NPB and NBPhen would result from an accumulation of electrons and holes at the interface. There will be a 200 mV or more injection barrier for electrons to surmount from the LUMO of NBPhen to NPB, and a 300 mV or more injection barrier for holes to overcome from the HOMO of NPB to NBPhen. Such interfacial recombination would emit closer to 360 nm. As such, it is likely the radiative recombination is occurring within NPB as opposed to the interfacial recombination shown in Fig.7.7. Note that the recombination signal strength, seen in Fig.7.5, is roughly between 1×10^{-6} 1×10^{-7} A_{rms}. We will see in the Organic Light Emitting Diode (OLED) recombination signal strength is 1-2 orders of magnitude higher.

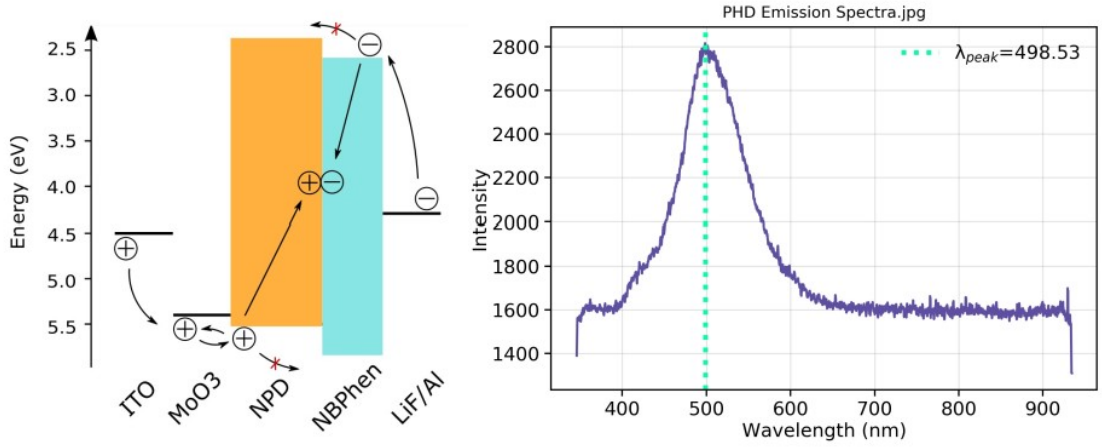

Figure 7.7: Left: Energy Diagram of PH diode, solid lines represent favorable paths for that charge carrier. Given the energy barriers for both electrons and holes into NBPhen and NPB respectively, recombination occurs at the planar interface. Right: Emission spectra of the PHD showing Intensity versus wavelength with the peak intensity wavelength indicated.

Higher Harmonic frequency Spectra of PH diode

As in the Hole Only device, SCLC is indicated in higher harmonic analysis by a vanishing third harmonic, seen in Fig.7.5. Looking at the PH diode higher harmonic measurements we see from 2.0-3.0 V forward bias the transition from exponential behavior, indicating recombination, to the vanishing third harmonic, indicating SCLC behavior being the MG2 quadratic dependence of voltage on current density.

Below 1×10^3 Hz we see significant, equally spaced harmonic signal, A_n, up to the 4th harmonic. Given the harmonic signal is proportional to the derivative of the transfer function we see that this signal fits for derivatives of the Shockley diode equation where the spacing between admittance signals , Y_n, is $\frac{1}{nk_BT}$. In taking the ratio of sequential harmonic admittance signals we may extract the diode ideality factor. The diode ideality of an Al/C60/CuPC/MoO_3/Ag PH diode was extracted by Larsen [16], seen in Fig.7.9, revealing a value of n=3, which was deemed reasonable

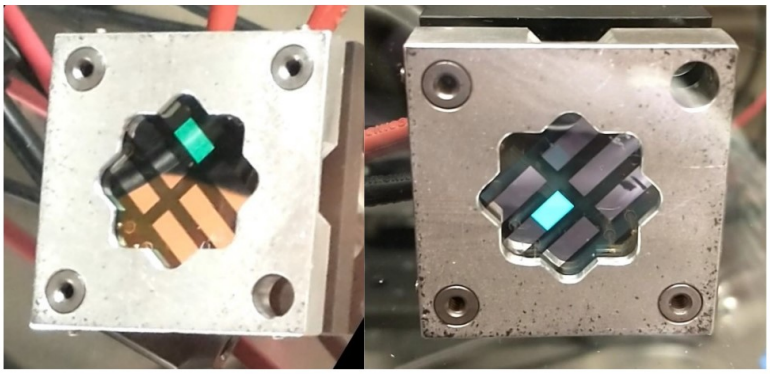

Figure 7.8: Left: OLED, Right: PHD showing device emission within sample holder. The OLED emits in the green while the PHD emits in the cyan.

,

for recombination at such a heterojunction interface.

The calculated diode ideality factor of the PHD is shown in Fig.7.10. In the JV curve of the PHD in Fig.7.10 left we see significant noise in the negative and injection voltage regimes below roughly 2 V, followed by exponential behavior (linear in the semilog), and a transport limited roll off at higher voltages. Fig.7.10 right shows the diode ideality factor, $n_{JV} = \left(\frac{kT}{q}\frac{\partial \ln J}{\partial V}\right)^{-1}$, as calculated from the slope of the JV curve. The mean and standard deviation, σ, of n as calculated from the Admittance spectra are shown as well. The green shaded regions indicate the voltage range where exponential behavior is observed in the Admittance spectra. Admittance spectra were measured at 50 mV_{rms} amplitude.

Since $n_{JV} \propto (\frac{\partial \ln J}{\partial V})^{-1}$, the zero slope of n_{JV} represents the zero curvature of Fig.7.10 left indicating linear behavior of the semilog curve. Therefore, the voltage of zero curvature of n_{JV} may be taken as representative of the device's exponential behavior, and consequently the most representative diode ideality factor as extracted derivative-wise from the semilog JV spectra. As expected, $n_{|Y_n|}$ shows strong agree-

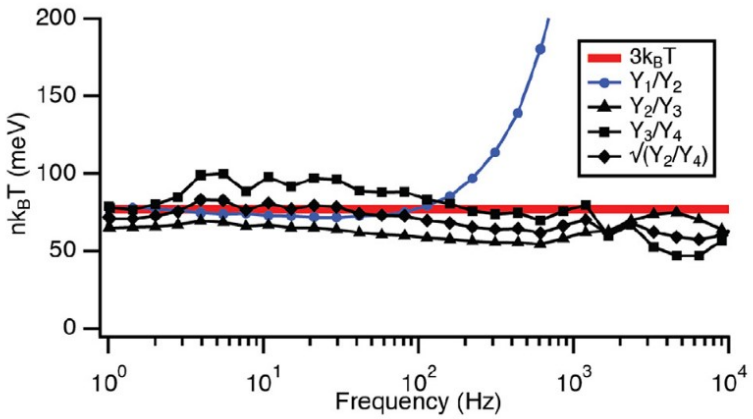

Figure 7.9: Sequential ratios of harmonic admittances as a function of frequency for a CuPc / C60 planar heterojunction device. [16]

ment with n_{JV} near the point of purely exponential behavior.

7.3 Organic Light Emitting Diode (OLED)

Next, we consider the Organic Light Emitting Diode (OLED). As in the PH diode, recombination occurs in the OLED device, however it will take place within the emitter layer AlQ3, as both holes and electrons can be injected from the NPB and NBPhen respectively, as seen in Fig.7.11. As such we expect to see faster recombination occurring than in the PH diode and an associated difference in the diode ideality factor.

The emission spectra of the AlQ3 OLED, Fig.7.11, shows a peak at 529.33 nm corresponding to a 2.34 eV transition. AlQ3 is reported to show photolumenescence at 512 nm (2.42 eV) in solution of THF. As with NPB, crystallization may act to further reduce this transition. As such a 2.34 eV transition aligns with expectations.

As in the PH diode the transition from diode to SCLC behavior is visible from 2.0-3.0 V forward bias, seen in Fig.7.12. Capacitive current turns on as expected near

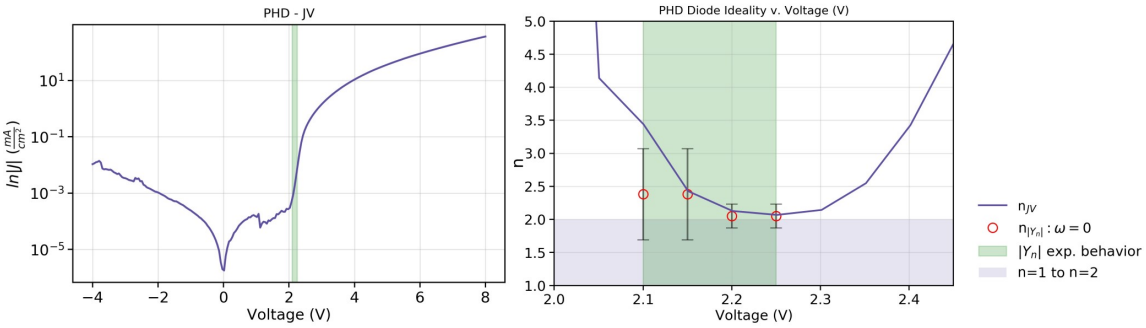

Figure 7.10: Left: PHD current density versus voltage (V) curve, the shaded green region indicates the voltage range where exponential behavior is observed in the same device's NLIS spectra. Right: Diode ideality versus voltage (V) for the PHD. The mean diode ideality factor extracted from the Admittance spectra measured at V_0=50 mV_{rms} is indicated by red circles with bars representing the standard deviation across Y_1/Y_3, Y_2/Y_4, etc. The $n = 1$ to $n = 2$ shaded region is a guide to the eye.

100 Hz in the first harmonic current and admittance.

However, recombination produces a much stronger signal, by 1-2 orders of magnitude, while the SCLC behavior signal strength remains on par with the PH diode. As in the PH diode, given the even harmonic signal spacing at moderate forward bias indicating exponential behavior, we may use the ratios of sequential harmonics to extract the diode ideality factor of the device.

In Fig.7.13 the current voltage spectra is plotted for the OLED where the shaded green region indicates the voltage range where exponential behavior is observed in the higher harmonic admittance spectra, and thus where the diode ideality factor may be calculated. Adjacent to the JV spectra, the diode ideality factor is plotted, as calculated from both the slope of the JV spectra, n_{JV}, and from the admittance spectra, $|Y_n|$ where red circles indicate the mean value at the low frequency limit and the bars indicate standard deviation across Y_1/Y_3, Y_2/Y_4, etc. $n_{|Y_n|}$ as $\omega \to 0$ shows strong agreement with n_{JV} of the DC regime as expected. The OLED shows a

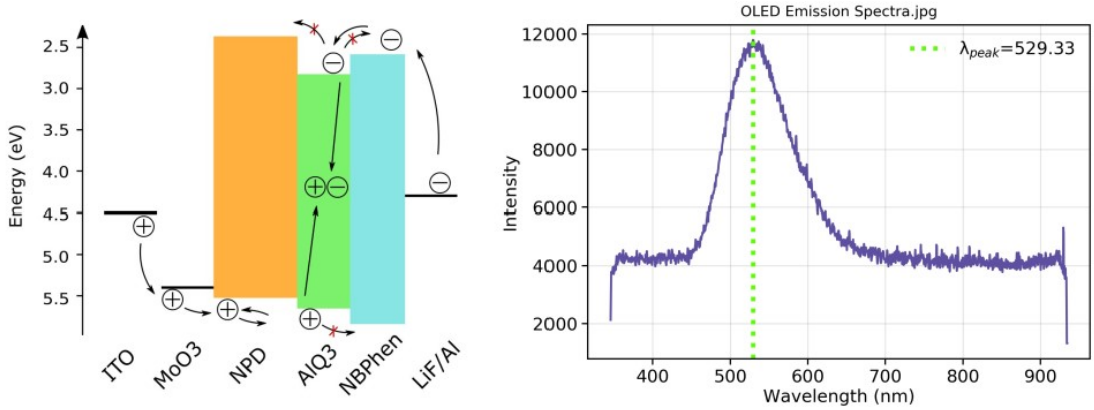

Figure 7.11: left: Energy Diagram of OLED; solid lines represent favorable paths for that charge carrier. Given the energy barriers for both electrons into NPB from AlQ3, recombination occurs within the AlQ3 emitter layer. Some leakage may occur for holes as they may favorably travel back to the NPB layer. right: OLED emission spectra showing a peak at 529.33 nm. The peak is indicated is its respective color.

wider recombination current limiting voltage regime than the PH diode, likely due to the presence of the AlQ3 recombination center within the OLED structure allowing recombination to occur over a wider voltage range.

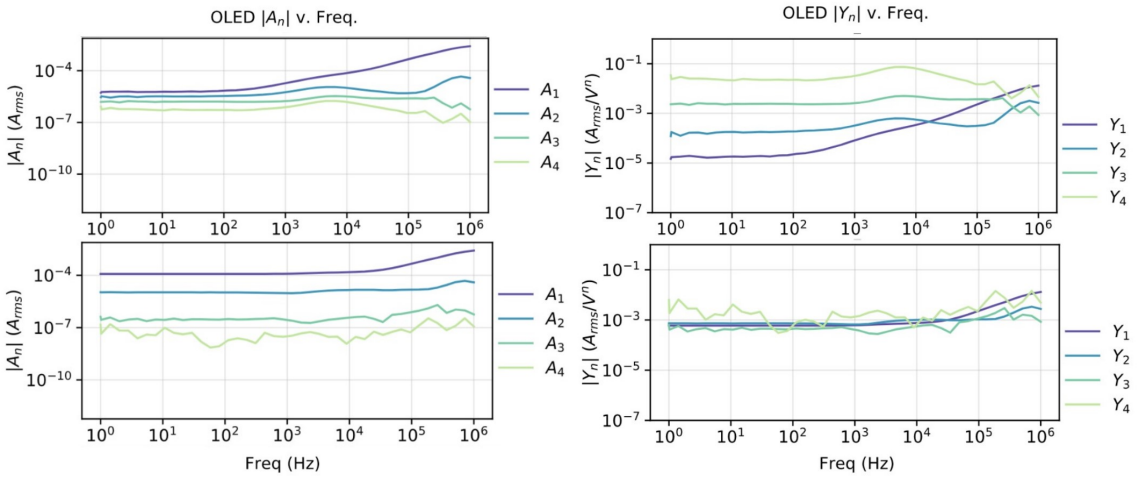

Figure 7.12: OLED Hole Only device, left: magnitude of the ac current, $|A_n|$ (Arms) v. Frequency (Hz), right: magnitude of the Admittance, $|Y_n|$ v. Frequency (Hz) for a 100 mV amplitude voltage excitation at 2.0 and 3.0 V applied dc bias. A_ns represent the Fourier coefficients the measured AC current at ω, 2ω, etc. where ω is the fundamental frequency defined by the AC voltage input signal. The first four harmonics are shown for both higher harmonic current and admittance.

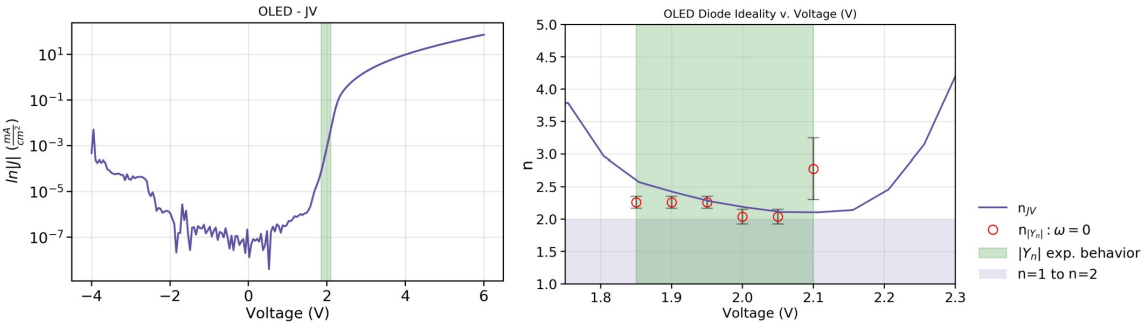

Figure 7.13: Left: OLED current density versus voltage (V) curve, the shaded green region indicates the voltage range where exponential behavior is observed in the same device's NLIS spectra. Right: Diode ideality versus voltage (V) for the PHD. The mean diode ideality factor extracted from the Admittance spectra measured at V_0=50 mV_{rms} is indicated by red circles with bars representing the standard deviation across Y_1/Y_3, Y_2/Y_4, etc. The $n = 1$ to $n = 2$ shaded region is a guide to the eye.

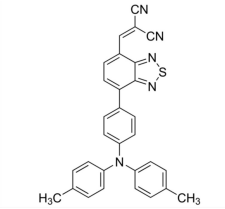

Figure 7.14: Chemical structure of DTDCPB

7.4 DTDCPB HO and SC devices

The above investigations have focused on primarily known systems being the NPB hole only device, the PH diode, and the OLED which serve to confirm the utility of NLIS to measure physical properties of devices and materials that are relatively well-studied in the literature. As NLIS is a new technique in this field, these results will lend credibility to our future efforts to measure nonlinear processes with unknown transfer functions. Our primary interests lie in OSCs with strong intramolecular charge transfer signatures that may lead to high dielectric constants and even free-carrier generation upon photoexcitation. We now extend our focus to 2-[(7-4-[N,N-Bis (4-methylphenyl) amino]phenyl-2,1,3-benzothiadiazol -4-yl)methylene] propanedinitrile (DTDCPB), Fig.7.14, which was recently shown by Nakayama et al. in collaboration with our group at UVM to have strong intramolecular charge transfer (CT) resulting in a low exciton binding energy (EBE).

As discussed in the Section 2.1, OSCs typically have low dielectric constants and consequently on photoexcitation produce bound charge excitons, rather than free carriers. The high binding energy of these excitons requires a donor-acceptor (D-A) interface to produce a charge transfer (CT) state which may transition into the charge separation (CS) state, shown diagrammatically in Fig.7.15, and dissociate into

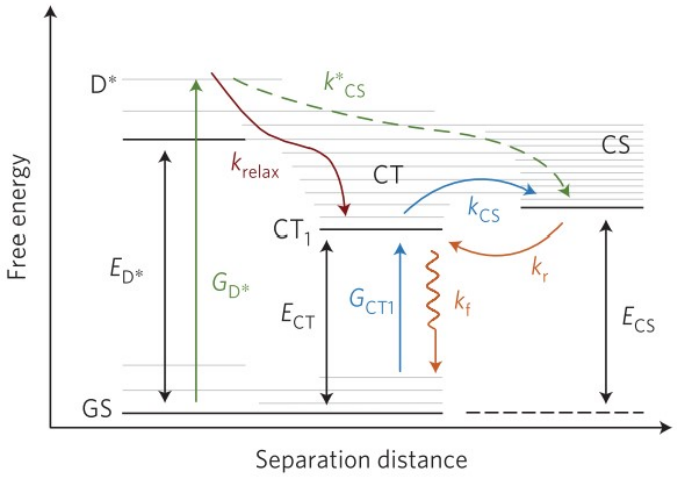

Figure 7.15: Energetic states at the donor acceptor O/O interface. Photons of energy higher than E_{D*} generate the excited donor state D which may generate a CS state by multiple paths. One is relaxation into the lowest energy thermally favorable CT state at rate constant k_{relax}, where CT_1 may radiatively decay to GS (k_f) or dissociate into the CS state (k_{CS}), the inverse occurring at rate (k_r). [32]*

free carriers to be collected by their respective electrodes. The planar bilayer OSC developed by Tang et al. [29] allowed for relatively ordered donor and acceptor layers to transport separated charges to their respective electrodes for collection. However, segregated donor and acceptor bulk results in low interfacial surface area for charge separation. The bulk heterojunction (BHJ) solar cell structure, first developed in 1995 by Yu et al., [41] aimed to enhance charge separation efficiency via a mixed phase D-A active layer. Pushing the heterojunction interface into the bulk provides spatially distributed interfacial surface area for charge separation between smaller donor and acceptor domains. This accommodates the short exciton diffusion length allowing more excitons to enter the CT state before recombining.

The BHJ design has proven highly successful, being used to bring OSC PCEs beyond 18% [42]. However, recent studies have investigated the inherent limitations

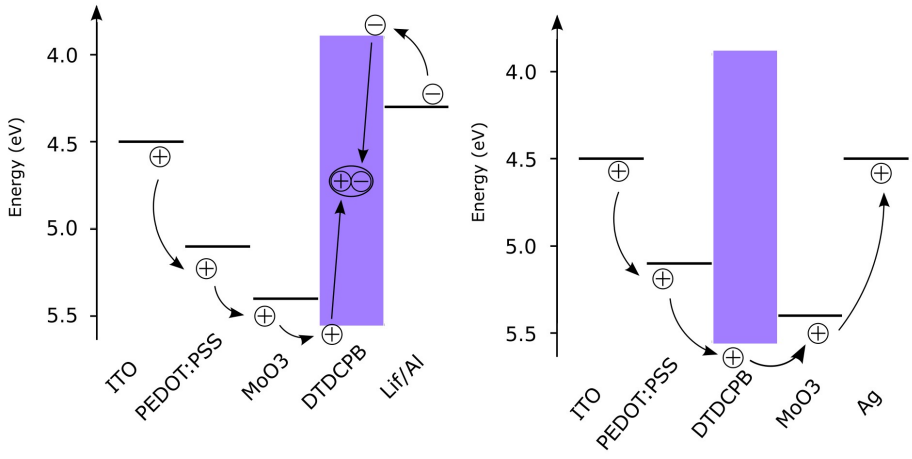

Figure 7.16: Energy Digram of the left: DTDCPB solar cell wherein recombination may occur, and right: DTDCPB hole only device where only holes are present. DTDCPB HOMO LUMO levels from [24].

to discrete D-A components, specifically energy loss due to the LUMO offset at the D-A interface [24]. As such, DTDCPB pushes the BHJ design even further by building the D-A interface into a single molecule where the CT state may be produced on photoexcitation due to the intramolecular dipole, bypassing the photon energy loss in the LUMO offset of a discrete D-A interface [24]. Once in the CT state, the exciton may be dissociated into free carriers at low energetic cost [32].

DTDCPB is a promising single component OPV molecule, wherein strong electron withdrawing and donating groups on the same molecule generate a large dipole moment promoting CT exciton formation on photoexcitation. In DTDCPB the triphenylamine donor is weakly positively polarized while the benzothiadiazole and malononitrile acceptors are weakly negatively polarized generating the intramolecular dipole. Specifically, the acceptor HOMO and donor LUMO overlap allowing exciton delocalization across the two, increasing the exciton Bohr radius and lowering the exciton binding energy below k_BT. This occurs at each discrete molecule, analogous

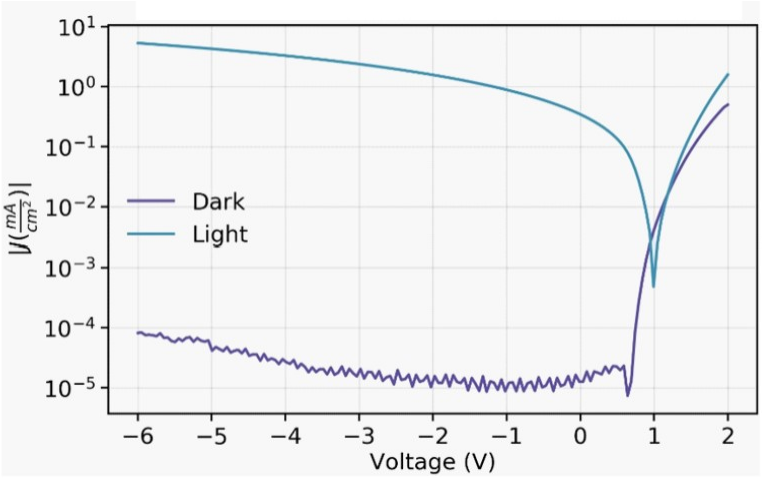

Figure 7.17: Light and dark current-voltage curves for the ITO / PEDOT:PSS / DTDCPB (100 nm) / MoO_3 (1 nm) / Al (100 nm) solar cell.

to the bulk photogeneration of silicon solar cells. By quantum solvation model and density functional theory calculations, Nakayama et al. as expected found DTDCPB to have an EBE well below k_BT [24].

We have fabricated hole only and solar cell (SC) devices using DTDCPB as the single active layer. As with the NPB HO devices, the DTDCPB HO structure uses the HTL MoO_3 to block electron injection from the cathode, while the DTDCPB SC structure allows electron injection for recombination DTDCPB, shown in Fig.7.16. Fig.7.17 shows the J-V characteristics for the DTDCPB SC in dark and under illumination. Shown in Fig.7.18, the DTDCPB SC under illumination transitions from the SCLC regime characteristic of a vanishing A_3 at 0.5 V to an exponential recombination limited current regime characteristic of significant A_n through at least the 4th harmonic, being the highest harmonic measured in this case. Using the NLIS technique, we have been able to extract a diode ideality factor under illumination of 2.75 from the Y_n spectra. However, given the small recombination regime voltage

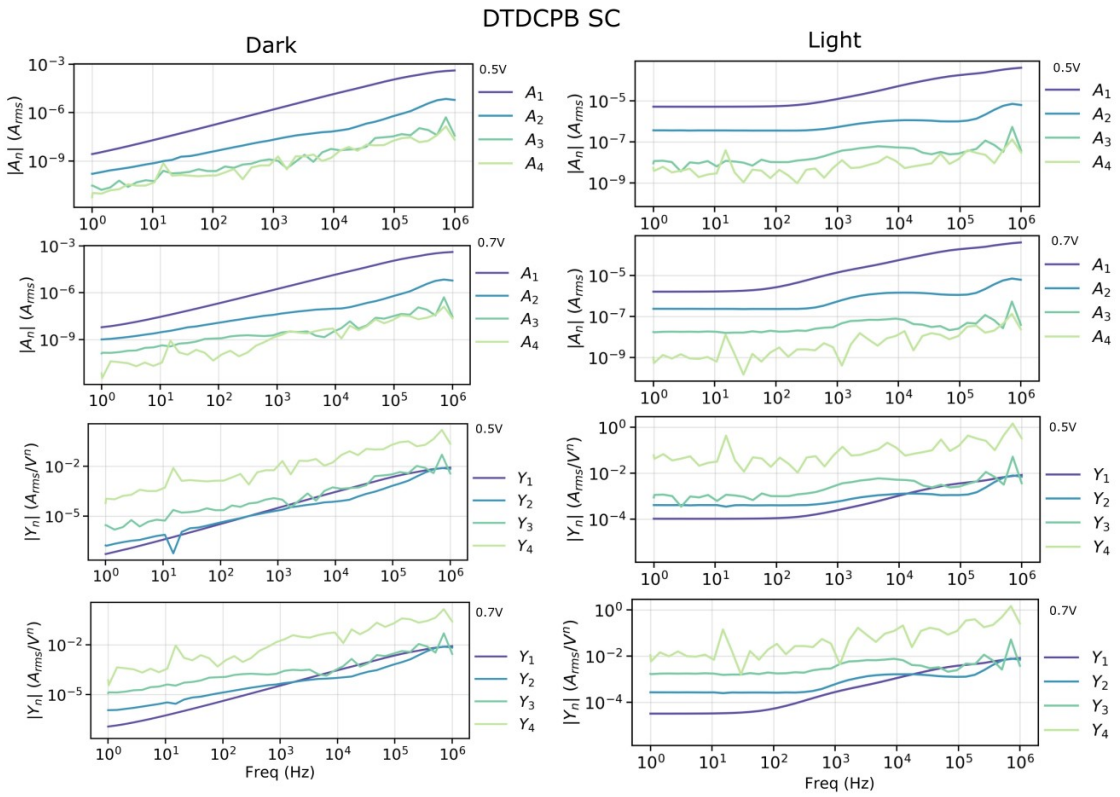

Figure 7.18: DTDCPB solar cell higher harmonic current and admittance in dark and under AM1.5G illumination showing behavior at 0.5 V and 0.7 V forward bias.

width of a solar cell the amplitude of the voltage input seems to be sampling into the injection and SCLC behavior making it difficult to accurately report the diode ideality factor from a measurement of purely recombination limited behavior. Future experiments will attempt to abate this issue by varying the voltage oscillation amplitude and perhaps expanding the recombination current limiting regime voltage width.

To calculate the carrier mobility the dielectric constant of DTDCPB was determined by capacitance-frequency spectroscopy at 0V in dark to be 2.74, and the mobility was calculated from the low frequency region of the magnitude of the second

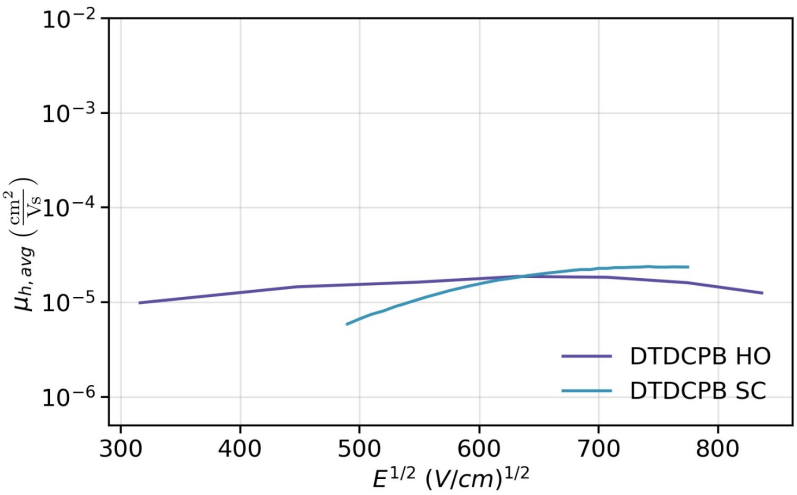

Figure 7.19: Hole mobility $\mu_{h,avg.}$ averaged over the low frequency 1-10 Hz range shown as a function of applied electric field $\sqrt{E}$ for both the hole only and solar cell DTDCPB devices as extracted from SCLC via the second harmonic current response. Both devices have a 100 nm DTDCPB layer thickness. Measurements were taken at 100 mV_{rms} oscillation amplitude in the dark.

harmonic Fourier coefficient of the alternating output current. Fig.7.19 shows the hole mobility $\mu_{h,avg.}$ averaged over the low frequency 1-10 Hz range shown as a function of applied electric field $\sqrt{E}$ for both the hole only and solar cell DTDCPB devices. Given the NLIS technique specifically measures the current limiting behavior, and we suspect recombination to occur near the LiF/DTDCPB interface, the current limiting process in the DTDCPB layer within the solar cell would be hole transport meaning the hole mobility was measured. This is confirmed by the HO device hole mobility measurement showing nearly identical behavior to the solar cell. To our knowledge no such measurement of hole mobility of DTDCPB has yet been reported.

Chapter 8

Conclusion

In this investigation, the higher harmonic response of a series of organic semiconductor based devices was investigated both in current and admittance frequency spectra. By employing a hole only device and selective layer thickness ratios in both a planar heterojunction diode and organic light emitting diode we have shown the second harmonic current response in the low frequency limit represents the second voltage derivative of the Mott-Gurney squared law. In using this relation to estimate the hole mobility of NPB across all three of these devices we show nonlinear impedance spectroscopy can definitively and accurately extract the hole mobility.

Further, we have used the higher harmonic admittance spectra to calculate the diode ideality factor within devices where charge carrier recombination occurs, being the PHD and OLED. We have shown, in correlation with extraction of the same parameter via the current density-voltage curves on the same respective device, very significant agreement between methods. As with the investigation of NPB hole mobility, the accuracy of diode ideality measurements further confirms the validity of the NLIS analytical method.

Finally, the NLIS technique was applied to a characterize DTDCPB, a promising intramolecular CT organic semiconductor for use in single layer OPV devices. Using a HO and SC device structure we have evaluated the diode ideality factor and hole mobility of DTDCPB. However, given the small recombination voltage width compared to the PHD and OLED, to confirm the accuracy of the diode ideality factor will require further investigation. The NLIS analytical technique has been validated through a series of baseline tests on known systems and a novel intramolecular charge transfer organic semiconductor has been evaluated with said technique.

Bibliography

[1] Sergei Baranovskii and Oleg Rubel. "Charge transport in disordered materials". In: *Springer Handbooks* (2017), p. 1. ISSN: 25228706. DOI: 10.1007/978-3-319-48933-9_9.

[2] H. Bässler. "Charge Transport in Disordered Organic Photoconductors a Monte Carlo Simulation Study". In: *Physica Status Solidi (B)* 175.1 (1993), pp. 15–56. ISSN: 15213951. DOI: 10.1002/pssb.2221750102.

[3] Heinz Bassler and Anna Kohler. "Charge Transport in Organic Semiconductors". In: *Springer* 310.October 2011 (2011), pp. 1–26. ISSN: 1726670X. DOI: 10.1007/128_2011_218. arXiv: /cactus.nci.nih.gov/download/nci/[http:].

[4] James C. Blakesley et al. "Towards reliable charge-mobility benchmark measurements for organic semiconductors". In: *Organic Electronics* 15.6 (2014), pp. 1263–1272. ISSN: 15661199. DOI: 10.1016/j.orgel.2014.02.008. URL: http://dx.doi.org/10.1016/j.orgel.2014.02.008.

[5] Ta Ya Chu and Ok Keun Song. "Hole mobility of N, N2032 -bis(naphthalen-1-yl)- N, N2032 -bis(phenyl) benzidine investigated by using space-charge-limited currents". In: *Applied Physics Letters* 90.20 (2007), pp. 1–4. ISSN: 00036951. DOI: 10.1063/1.2741055.

[6] Ta Ya Chu and Ok Keun Song. "Thickness dependence of the trap states in organic thin film of N, N2032 -bis(naphthalen-1-yl)- N, N2032 -bis(phenyl) benzidine". In: *Applied Physics Letters* 91.7 (2007), pp. 1–4. ISSN: 00036951. DOI: 10.1063/1.2771536.

[7] K. Darowicki and J. Orlikowski. "Fast method for the determination of the charge transfer coefficient of an electrode reaction". In: *Electrochimica Acta* 44.2-3 (1998), pp. 433–436. ISSN: 00134686. DOI: 10.1016/S0013-4686(98)00052-8.

[8] Fathima Fasmin and Ramanathan Srinivasan. “Review—Nonlinear Electrochemical Impedance Spectroscopy”. In: *Journal of The Electrochemical Society* 164.7 (2017), H443–H455. ISSN: 0013-4651. DOI: 10.1149/2.0391707jes.

[9] N. C. Giebink et al. “Ideal diode equation for organic heterojunctions. I. Derivation and application”. In: *Physical Review B* 82.15 (2010), pp. 1–12. ISSN: 1098-0121. DOI: 10.1103/physrevb.82.155305.

[10] Gabriel González. “Quantum theory of space charge limited current in solids”. In: *Journal of Applied Physics* 117.8 (2015), pp. 1–4. ISSN: 10897550. DOI: 10.1063/1.4913512. arXiv: 1411.4659. URL: http://dx.doi.org/10.1063/1.4913512.

[11] Martin A. Green et al. “Solar cell efficiency tables (Version 55)”. In: *Progress in Photovoltaics: Research and Applications* 28.1 (2020), pp. 3–15. ISSN: 1099159X. DOI: 10.1002/pip.3228.

[12] Brian A. Gregg, Si Guang Chen, and Russell A. Cormier. “Coulomb forces and doping in organic semiconductors”. In: *Chemistry of Materials* 16.23 (2004), pp. 4586–4599. ISSN: 08974756. DOI: 10.1021/cm049625c.

[13] Hamna F. Haneef, Andrew M. Zeidell, and Oana D. Jurchescu. “Charge carrier traps in organic semiconductors: A review on the underlying physics and impact on electronic devices”. In: *Journal of Materials Chemistry C* 8.3 (2020), pp. 759–787. ISSN: 20507526. DOI: 10.1039/c9tc05695e.

[14] David A. Harrington. “Theory of electrochemical impedance of surface reactions: second-harmonic and large-amplitude response”. In: *Canadian Journal of Chemistry* 75.11 (1997), pp. 1508–1517. DOI: https://doi.org/10.1139/v97-181. URL: http://library1.nida.ac.th/termpaper6/sd/2554/19755.pdf.

[15] Wei Lai. “Electrochimica Acta Fourier analysis of complex impedance (amplitude and phase) in nonlinear systems : A case study of diodes”. In: *Electrochimica Acta* 55.19 (2010), pp. 5511–5518. ISSN: 0013-4686. DOI: 10.1016/j.electacta.2010.04.016. URL: http://dx.doi.org/10.1016/j.electacta.2010.04.016.

[16] Andrew Larsen et al. “Nonlinear impedance spectroscopy of organic MIS capacitors and planar heterojunction diodes”. In: *Organic Electronics* 62.July (2018), pp. 660–666. ISSN: 15661199. DOI: 10.1016/j.orgel.2018.07.003. URL: https://doi.org/10.1016/j.orgel.2018.07.003.

[17] Haoyuan Li et al. “Charge transport in amorphous organic semiconductors: Effects of disorder, carrier density, traps, and scatters”. In: *Israel Journal of Chemistry* 54.7 (2014), pp. 918–926. ISSN: 18695868. DOI: 10.1002/ijch.201400057.

[18] Vadim F. Lvovich and Matthew F. Smiechowski. “Non-linear impedance analysis of industrial lubricants”. In: *Electrochimica Acta* 53.25 (2008), pp. 7375–7385. ISSN: 00134686. DOI: 10.1016/j.electacta.2007.12.014.

[19] Dongge Ma. *Organic semiconductor heterojunction and its application in organic light-emitting diodes (Conference Presentation)*. 2016, p. 32. ISBN: 9783662536933. DOI: 10.1117/12.2239059.

[20] J Ross Macdonald and William B. Johnson. “1. Fundamentals of Impedance Spectroscopy”. In: *Impedance Spectroscopy: Theory, Experiment, and Applications, Second Edition*. 2005, pp. 1–26. ISBN: 0471647497. DOI: 10.1002/0471716243.ch1.

[21] Toshinori Matsushima, Yoshiki Kinoshita, and Hideyuki Murata. “Formation of Ohmic hole injection by inserting an ultrathin layer of molybdenum trioxide between indium tin oxide and organic hole-transporting layers”. In: *Applied Physics Letters* 91.25 (2007), pp. 10–13. ISSN: 00036951. DOI: 10.1063/1.2825275.

[22] Matthew D. Murbach, Victor W. Hu, and Daniel T. Schwartz. “Nonlinear Electrochemical Impedance Spectroscopy of Lithium-Ion Batteries: Experimental Approach, Analysis, and Initial Findings”. In: *Journal of The Electrochemical Society* 165.11 (2018), A2758–A2765. ISSN: 0013-4651. DOI: 10.1149/2.0711811jes.

[23] Shigeki Naka et al. “Carrier transport properties of organic materials for EL device operation”. In: *Synthetic Metals* 111 (2000), pp. 331–333. ISSN: 03796779. DOI: 10.1016/S0379-6779(99)00358-6.

[24] Ken Ichi Nakayama et al. “Single-component organic solar cells based on intramolecular charge transfer photoabsorption”. In: *Materials* 14.5 (2021), pp. 1–12. ISSN: 19961944. DOI: 10.3390/ma14051200.

[25] N. D. Nguyen, M. Schmeits, and H. P. Loebl. “Determination of charge-carrier transport in organic devices by admittance spectroscopy: Application to hole mobility in α -NPD”. In: *Physical Review B - Condensed Matter and Materials Physics* 75.7 (2007), pp. 1–13. ISSN: 10980121. DOI: 10.1103/PhysRevB.75.075307.

[26] NREL. *Best Research-Cell Efficiency Chart.pdf*. 2019. URL: https://www.nrel.gov/pv/assets/pdfs/best-research-cell-efficiencies.20190802.pdf.

[27] Matthew F. Smiechowski et al. "Non-linear impedance characterization of blood cells-derived microparticle biomarkers suspensions". In: *Electrochimica Acta* 56.23 (2011), pp. 7763–7771. ISSN: 00134686. DOI: 10.1016/j.electacta.2011.03.116. URL: http://dx.doi.org/10.1016/j.electacta.2011.03.116.

[28] Jun Ichi Takahashi. "Negative impedance of organic light emitting diodes in AC electrical response". In: *Journal of Applied Physics* 125.24 (2019). ISSN: 10897550. DOI: 10.1063/1.5094562.

[29] C. W. Tang. "Two-layer organic photovoltaic cell". In: *Applied Physics Letters* 48.2 (1986), pp. 183–185. ISSN: 00036951. DOI: 10.1063/1.96937.

[30] J. X. Tang, C. S. Lee, and S. T. Lee. "Electronic structures of organic/organic heterojunctions: From vacuum level alignment to Fermi level pinning". In: *Journal of Applied Physics* 101.6 (2007), pp. 1–5. ISSN: 00218979. DOI: 10.1063/1.2710297.

[31] Brian J Thompson and New York. *OPV___mechanism___materials___and_devices*. 2005. ISBN: 9780824759636.

[32] Koen Vandewal et al. "Efficient charge generation by relaxed charge-transfer states at organic interfaces". In: *Nature Materials* 13.1 (2014), pp. 63–68. ISSN: 14761122. DOI: 10.1038/nmat3807. URL: http://dx.doi.org/10.1038/nmat3807.

[33] J. R. Wilson, D. T. Schwartz, and S. B. Adler. "Nonlinear electrochemical impedance spectroscopy for solid oxide fuel cell cathode materials". In: *Electrochimica Acta* 51.8-9 (2006), pp. 1389–1402. ISSN: 00134686. DOI: 10.1016/j.electacta.2005.02.109.

[34] Jamie R. Wilson et al. "Measurement of oxygen exchange kinetics on thin-film La 0.6Sr0.4CoO3-δ using nonlinear electrochemical impedance spectroscopy". In: *Electrochemical and Solid-State Letters* 10.5 (2007), pp. 81–86. ISSN: 10990062. DOI: 10.1149/1.2710178.

[35] Mariusz Wojcik, Irmina Zawieja, and Kazuhiko Seki. "Charge Transport in Disordered Organic Solids: Refining the Bässler Equation with High-Precision Simulation Results". In: *Journal of Physical Chemistry C* 124.33 (2020), pp. 17879–17888. ISSN: 19327455. DOI: 10.1021/acs.jpcc.0c03064.

[36] Danny K.Y. Wong and Douglas R. MacFarlane. "Harmonic impedance spectroscopy. Theory and experimental results for reversible and quasi-reversible redox systems". In: *Journal of Physical Chemistry* 99.7 (1995), pp. 2134–2142. ISSN: 00223654. DOI: 10.1021/j100007a051.

[37] Hui Xu et al. "Thickness Dependence of Carrier Mobility and the Interface Trap Free Energy Investigated by Impedance Spectroscopy in Organic Semiconductors". In: *Journal of Physical Chemistry C* 120.31 (2016), pp. 17184–17189. ISSN: 19327455. DOI: 10.1021/acs.jpcc.6b03964.

[38] Ning Xu. "Nonlinear Impedance Spectroscopy and Its Applications to Solid Oxide Fuel Cells". In: (2012).

[39] Ning Xu and D. Jason Riley. "Nonlinear analysis of a classical system: The Faradaic process". In: *Electrochimica Acta* 94 (2013), pp. 206–213. ISSN: 00134686. DOI: 10.1016/j.electacta.2013.01.141. URL: http://dx.doi.org/10.1016/j.electacta.2013.01.141.

[40] Y. F. Xu et al. "Impedance spectroscopy study on transport properties of N,N2032-diphenyl-N,N2032-bis(1-naphthyl)-1,12032-biphenyl-4, 42032-diamine". In: *Physica B: Condensed Matter* 362.1-4 (2005), pp. 35–40. ISSN: 09214526. DOI: 10.1016/j.physb.2005.01.472.

[41] G. Yu et al. "Polymer Photovoltaic Cells: Enhanced Efficiencies via a Network of Internal Donor-Acceptor Heterojunctions". In: *Science* 270 (1995), pp. 1–3. URL: http://science.sciencemag.org/.

[42] Ming Zhang et al. "Single-layered organic photovoltaics with double cascading charge transport pathways: 18% efficiencies". In: *Nature Communications* 12.1 (2021), pp. 1–10. ISSN: 20411723. DOI: 10.1038/s41467-020-20580-8. URL: http://dx.doi.org/10.1038/s41467-020-20580-8.